DISSERTATION

ESTIMATION AND CORRECTION OF WET ICE ATTENUATION FOR X-BAND RADAR

Submitted by:

Leyda V. León Colón

Department of Electrical and Computer Engineering

In partial fulfillment of the requirements

For the Degree of Doctor of Philosophy

Colorado State University

Fort Collins, Colorado

Summer 2010

COLORADO STATE UNIVERSITY

July 9, 2010

WE HEREBY RECOMMEND THAT THE DISSERTATION PREPARED UNDER OUR SUPERVISION BY LEYDA V LEON COLON ENTITLED ESTIMATION AND CORRECTION OF WET ICE ATTENUATION FOR X-BAND RADAR BE ACCEPTED AS FULFILLING IN PART REQUIREMENTS FOR THE DEGREE OF DOCTOR OF PHILOSOPHY.

Committee on Graduate Work

V. Chandrasekar

Steve C. Reising

Steve Rutledge

Advisor: V.N. Bringi

Department Head: Anthony A. Maciejewski

ABSTRACT OF DISSERTATION

ESTIMATION AND CORRECTION OF WET ICE ATTENUATION FOR X-BAND RADAR

In the past, single polarized X-band radars were primarily used (along with S-band radars) for hail detection, first by the Russians and then later for the National Hail Research Experiment (NHRE). But X-band radars were not used alone because of the large attenuation at frequencies around 10 GHz and higher, until dual-polarized radars were developed. This fact has brought attention to development and evaluation of correction techniques for rain attenuation in order to exploit the advantages of dual-polarized data. Past developed methods make use of the close relation between the differential propagation phase Φ_{DP} and path attenuation *PIA*. Their use is known to be successful in rain events, but in the presence of wet ice, these methods are no longer useful because the differential propagation phase is not affected by the isotropic wet ice. This factor was the basis to develop herein two different techniques for estimating the attenuation due to rain and wet ice separately and correct for the wet ice induced attenuation**.**

In this dissertation, two methods are investigated and evaluated. The first method uses the Surface Reference Technique (*SRT*) α-adjustment method to correct for the attenuation. This method was first developed for the Tropical Rainfall Measuring Mission (TRMM) precipitation radar. We assume that S-band data is un-attenuated and is used as a reference. The difference in reflectivities at the end of the beam (defined as the average of the last ten gates with 'good' data) is attributed to the total attenuation (sum of rain and any wet ice) along the propagation path. The attenuation due to the rain component, if any, is corrected for using the differential propagation phase. Then the α value in the $A_h(X)^{wet\ ice}$-$Z_h(X)$ power law relationship (with fixed exponent β) is

adjusted such that the reflectivities at S-band and the rain-corrected reflectivity at X-band at the end of the beam are forced to match. This adjusted α is used to apportion the reflectivity backwards, which assumes the α parameter is constant along the beam. Using the adjusted value, the attenuation due to wet ice is estimated separately from that of rain. This method is termed here as the *SRT*-modified correction method.

This method has been applied to different datasets. It was evaluated in both simulated and measured radar data. Using the Regional Atmospheric Modeling System (RAMS) model a supercell was simulated by Professor's Cotton's group at Colorado State University (CSU). A radar emulator was used to simulate radar measurements from this supercell at both X-band and S-bands. Results showed good agreement of both corrected reflectivity profiles and wet ice specific attenuation estimation. A dataset from the International H2O Project (IHOP) that had rain mixed with wet ice particles (mixed phase region) was analyzed too. It showed good agreement also, when comparing profiles; moreover wet ice attenuation contours showed agreement with high values of reflectivity as expected in wet ice regions. Data collected by the Center for Adaptive Sensing of the Atmosphere (CASA) radar network was analyzed along with both Next Generation Radars (NEXRAD) KTLX and KOUN data. For the light rain event (CASA/KTLX), the dual wavelength ratio at the maximum range was close to unity as expected for Rayleigh scattering. When corrected for wet ice, the specific attenuation showed agreement with high values in reflectivity at both bands. Finally, this method was applied to two different Cloud Physics Radar (CP2) radar data sets. In the CP2 data analysis, Mie hail signals were eliminated for the purpose of this research. Results from both datasets showed that resulting corrected reflectivity was comparable to the un-attenuated S-band data.

Given that an un-attenuated reference signal, like the one described before, might not always be available, a second method was developed without this assumption. This second method estimates the wet ice specific attenuation using a $A_h(X)^{wet\ ice}$-$Z_h(X)$ power law relation with

fixed coefficients. These fixed coefficients were retrieved using the same CP2 datasets and compared with previous findings. Then, assuming that the reflectivity is already corrected for rain attenuation, the Hitschfeld-Bordan forward correction method is used. To determine the areas where the correction method will be applied the Hydrometeor Identification (HID) algorithm was used. The HID data is used here to locate the first 'good' range gate of the mixed phase region containing the wet ice. This method is termed as the Piece-Wise Forward correction method (*PWF*).

Similar to the first method, this second method was applied to different datasets. First it was applied to one of the two CP2 datasets available, where the Mie 'hail' signal was eliminated. The resulting corrected reflectivity showed good agreement compared with the S-band un-attenuated reflectivity. Also this method was applied to the same convective dataset (from CASA) as the one previously analyzed with the *SRT*-modified method. It presented higher reflectivity values in wet ice identified areas, but lower values than those presented by the *SRT*-modified method. The results were also compared with the Networked Based (*NB*) method.

Leyda V. León Colón
Electrical and Computer Engineering Department
Colorado State University
Fort Collins, CO, 80523
Summer 2010

ACKNOWLEDGEMENTS

I am deeply grateful to my advisor, Dr. V.N. Bringi, for his knowledge, guidance, encouragement, and support during my graduate studies. I would also like to thank my Co-Advisor Dr. V. Chandrasekar for his encouragement and support and to Dr. Steve C. Reising and Dr. Steve Rutledge for serving as my committee members, for their corrections, suggestions and support.

I would also like to thank everyone in the Radar and Communication Laboratory for their help and friendship, especially Dr. G.J. Huang and Dr. Brenda Dolan for their insights, time and help.

I am enormously grateful to my parents, Leida A. Colón and Ramón E. León, my sister, Carmen G. León, my parents-in-law, Irene Olivo and Félix R. Ortiz, my brother in law, Félix R. Ortiz, and all my family, for their love, support and encouragements throughout this journey.

Finally and foremost, I would like to express my deep appreciation to my husband José R. Ortiz and my son Robert E. Ortiz for their patience, love, support, and encouragement, which made this journey an unbelievable one.

This research was supported by the NSF (ERC-0313747).

LIST OF TABLES

LIST OF FIGURES

TABLE OF CONTENTS

CHAPTER I

I. INTRODUCTION

X-band radars have been used to sense the atmosphere since the early 1950's. In the early 1970's dual-wavelength (S/X) band radars were developed in the US for hail detection and possible mitigation of large hail production following early Russian work (Sulakvelidze 1965). The National Hail Research Experiment (NHRE) was conducted in North Eastern Colorado in the early-mid 70's using two dual-wavelength radars (CP2 and CHILL) (Atlas and Ludlam 1961; Eccles and Atlas 1973; Jameson and Heymsfield 1980; Tuttle and Rinehart 1983). After NHRE, it was concluded that it was not possible to mitigate large hail production by cloud seeding. There was a lull in the use of X-band weather radars due to large attenuation in rain until recently when dual-polarized radars became available. However, the use of S-band and C-band radars to study all types of precipitation has been preferred over X-band since they do not experience as much attenuation because of the larger wavelength.

In 2003, a new National Science Foundation Engineering Research Center (NSF-ERC), CASA, was established in order to sense the lower atmosphere not observed by the current NEXRAD Weather Surveillance Radar (WSR-88D) network. With the CASA ERC, a low cost and dynamic adaptive network was developed whereby lower atmospheric hazardous weather events could be detected with high resolution (McLaughlin et al. 2005; Brotzge et al. 2005). The scan parameters of these dual polarized radars can be dynamically adapted in real-time to changing weather conditions. The first CASA test-bed (Integrative Project 1, or IP1) was established in the southwest of Oklahoma (in the cities of Rush Spring, Chickasha, Cyril, and Lawton) in May

2006. Four 2° beam-width radars have been placed 30 km apart from each other with a maximum unambiguous range of 30-40 km and range resolution of 150 m. They have been operational and collecting data for several years since then.

The use of meteorological radars with shorter wavelength brings up the long studied attenuation problem. A dual polarization technique is applied in real time for each beam (Liu et al. 2006a), Park et al. 2005) to correct for attenuation. This way, real-time attenuation-corrected reflectivity and differential reflectivity are available for dissemination to researchers, the National Weather Service (NWS), industrial partners, and emergency managers.

Methods to correct for rain attenuation use the close relation between the differential propagation phase Φ_{dp} and path attenuation *PIA*. This relation is the basis of these correction methods where Φ_{dp} is involved either directly or as a constraint (a review of them is well explained in Part et al. 2003a). The use of these methods is known to be successful in rain events, but when wet ice is present along the path, e.g. melting graupel, hail below the 0°C level or hail in wet growth above the 0°C level, this method is no longer useful because the differential propagation phase is not affected by the isotropic wet ice. This led us to develop a technique for estimating the attenuation due to rain and wet ice separately and to correct for the wet ice induced attenuation**.**

Battan (1971) used the Mie theory to calculate the radar attenuation of wet ice spheres for S, C and X bands. He found that significant attenuation can be caused when a thin water layer surrounds the ice particle (e.g. hail) and that the effect was larger at shorter wavelengths (Atlas et al. 1960 have also studied this effect). In part, these studies have been of great importance in the past for the selection of wavelength for meteorological radars, e.g. the use of S-band and C-band rather than X-band. The attenuation due to wet ice is difficult to correct, even for polarimetric radars. The impact it has on radar parameters such as reflectivity can be very high in deep convection. Raindrops form a highly oriented medium while here we assume the wet ice as

isotropic particles. To quantify this attenuation, along with its vertical extent above the freezing level (separately from the rain attenuation), can help to understand the microphysical processes involved within rapidly evolving convective storms as well as *A*-*Z* relationships.

In the past, the wet ice attenuation was either ignored or skipped in the analyses. Tuttle and Rinehart (1983) used an S/X-band dual-wavelength radar system for hail detection after correcting for attenuation. In many hailstorms that they analyzed, the attenuation was so high in the core that X-band reflectivity fell below the receiver noise threshold and some other areas showed up to 30 dB in attenuation. There was likely to be hail present within the storm core and in these regions attenuation was not calculated, though they proposed to flag these to not be used in their analysis. Vulpiani et al. (2007) implemented an adaptive attenuation correction method based on Φ_{dp} with an embedded Fuzzy-Logic hydrometeor classification to an extreme convective event (at C-band), in which the mixed phase region was evaluated. In Tabary et al. (2008) unusually large C-band attenuation was observed and retrieved rainfall rates (R) were flagged as error prone where wet ice was present. This is mostly done because reflectivities must be as accurate to within 1 dB for quantitative estimation of rainfall rates using *Z*-*R* relations.

Here, we have developed two methods for correcting the attenuation due to wet ice. The first one uses a surface reference technique (*SRT*-modified) that was first implemented with simulated radar data. The CSU RAMS model provided microphysics parameters that were used to emulate radar scanning at both X-band and S-band frequencies using a T-matrix scattering based program. When examining the rays intercepting the wet ice regions, it was clearly shown that the Φ_{dp}-based methods for attenuation correction were not correcting all the attenuation induced in the X-band signal. The *SRT*-modified method was implemented with good results where the attenuation due to rain and wet ice were estimated separately. The same technique was implemented for other data sets, e.g., from IHOP, the CASA/NEXRAD data, and CP2 data. A second method was

developed, in which the correction was performed in a piece-wise forward way (*PWF*). It is based on a fixed *A*-*Z* relationship and does not depend on an un-attenuated reference. An HID algorithm was used to identify where the correction was going to be implemented and a forward method of correction using the Hitschfeld-Bordan solution for attenuation correction was used. This method was implemented using CP2 and CASA data where the attenuation due to wet ice was estimated and corrected for.

A. Dissertation Organization

This dissertation is organized in five chapters as follows:

Chapter 1: INTRODUCTION

In the Introduction chapter, the problem is described along with some references to past related research. The descriptions of the Data Sources used to develop the new methods for the wet ice attenuation corrections are also included in this chapter along with the research objectives.

Chapter 2: BACKGROUND THEORY

In the Background Theory chapter, much of the necessary theory related to this research is described. The different sections include a review of radar theory, the radar signal interaction with hydrometeors, the radar signal attenuation with correction methods and finalizes with a section on the *A*-*Z* relationships.

Chapter 3: WET ICE ATTENUATION CORRECTION WITH SRT MODIFIED METHOD

In this chapter the wet ice attenuation estimation and correction using the *SRT*-modified method is described. The results when implementing the CSU RAMS supercell simulation, IHOP's X-band and S-band polarimetric radars (XPOL and SPOL), CASA/NEXRAD, and CP2 data, described in Chapter 1, are presented and analyzed.

Chapter 4: WET ICE ATTENUATION CORRECTION USING PIECE-WISE FORWARD METHOD

In the fourth chapter, a second wet ice attenuation estimation and correction method is examined using the *PWF* method without using an un-attenuated reference. The results using CP2 and CASA/NEXRAD datasets, described in Chapter 1, are also presented and analyzed.

Chapter 5: SUMMARY AND FUTURE WORK

This chapter summarizes the results found and discussed in Chapters 2 and 3 and proposes future work that can be implemented to continue this research.

B. Data Sources

To test the techniques, four different data sets have been analyzed so far. They are, (i) a RAMS supercell event simulation, (ii) an event in which rain is mixed with wet ice, collected by the XPOL and SPOL radars on June 16, 2002 during the IHOP campaign, (iii) a stratiform and a convective event passing through the CASA network on June 20th, 2007 and on June 10th, 2007 respectively, and finally (iv) two events from the CP2 radar in Brisbane on March 26, 2008 and October 21st, 2007.

i. RAMS

A supercell was simulated using the RAMS 2-moment microphysical parameterization described in Meyers et al. (1997). It predicts number concentrations N_t and mixing ratios r_{mix} of different species like rain, hail and graupel. The gamma distribution is used with shape parameter ν equal to 2. The temperature along with the predicted N_t and r_{mix} are provided at each grid point. These

predicted values are used in a radar emulator that uses a T-matrix scattering code at each grid point along with assumptions about particle shapes, orientations and dielectric constants.

For the rain case, the assumed intercept parameter N_o is fixed to the Marshall-Palmer value of 8000 $mm^{-1}m^{-3}$. The raindrops are assumed to be oblate with the equilibrium axis ratios given by Beard and Chuang (1987) shape model. Also the canting angle is assumed to be Gaussian in shape with standard deviation of 5°. For the hail/graupel case, it is assumed that they are oblate in shape with axis ratio of 0.8 with random orientation. The distinction of dry and wet ice is done by using the liquid fraction given by the RAMS model. Polarimetric radar variables at X-band are calculated such as reflectivity (Z_h), specific differential phase (K_{dp}) and also the specific total attenuation (A_h) as well as the attenuation contributions from each particle type ($A_{h\ rain}$, $A_{h\ dry\text{-}ice}$, $A_{h\ \text{wet-ice}}$, $A_{h\ \text{graupel}}$). For the S-band case, only the reflectivity (Z_h) profiles are used here.

With these gridded data, range height indicator (RHI) and plan position indicator (PPI) scans were simulated for both frequencies. The system characteristics used to simulate the radar scans are described in Table 1.1.

Table 1.1: RAMS supercell: radar system characteristics used for the scan simulation.

RADAR SIMULATED	X-BAND	S-BAND
Frequency	9.8 GHz	3 GHz
Polarization	Linear H and V	Linear H and V
Half Power Beam Width (HPBW)	1.8°	1.1°
Range Resolution	100 m	150 m
Maximum Range	30 km	150 km
Simulated Variables	Z, Z_{dr}, Φ_{dp}, ρ_{hv}	Z, Z_{dr}, Φ_{dp}, ρ_{hv}

ii. IHOP

The IHOP data analyzed herein corresponds to an event on June 16, 2002 from the IHOP 2002 campaign. The XPOL/SPOL datasets include PPI scans at different elevation angles (0.5 º to 10.5º). This dataset provides X-band dual-polarized radar data as well as S-band reflectivity data (note, even though SPOL radar is dual-polarized, no polarimetric variable is used other than the reflectivity). Note also, that the two radars are separate systems on different pedestals, unlike the CP2 radar where only one pedestal is used. These radar data were analyzed in the same way as the RAMS supercell simulation dataset. The XPOL and SPOL system characteristics are described in Table 1.2.

Table 1.2: IHOP's XPOL and SPOL radar systems.

RADAR	XPOL	SPOL
Frequency	10 GHz	3 GHz
Polarization	Simultaneous Linear H and V	Linear H and V
Half Power Beamwidth (HPBW)	0.95°	1°
Range Resolution	150 m	150 m
Maximum Range	60 km	150 km
Measured Variables	Z, Φ_{dp}	Z, Z_{dr}, Φ_{dp}, ρ_{hv},

iii. CASA/KTLX and CASA/KOUN

The CASA radar network, operating at X-band, was deployed in Oklahoma during the spring of 2007. During this period two events are considered as described below.

A stratiform rain event passing through the CASA Testbed on 20 June 2007 around 10:00 UTC was studied. Radar volume data from the NEXRAD KTLX, located in Oklahoma City, is used as a reference. A 2° elevation angle PPI scan is considered.

A convective event on 10 June 2007 passing through the CASA radar network around 23:47 UTC showed excess attenuation after being corrected for rain implying the presence of hail. The National Center for Atmospheric Research (NSSL) Polarimetric NEXRAD radar (KOUN) located in Norman, Oklahoma, provided S-band data for the same storm. Comparisons between CASA and KOUN data revealed differences between rain attenuation-corrected X-band reflectivity and the un-attenuated S-band reflectivity of up to 35 dB. A hydrometeor identification algorithm at S-band was applied at a height of 6.5 km which showed the presence of high density graupel (wet ice) aloft in the areas where the high attenuation was observed. A PPI scan at 12.24° in elevation of the Cyril (KCYR) radar is considered to obtain the beams passing through the wet ice region aloft. The system characteristics for the CASA, KOUN and KTLX radars are described in Table 1.3.

Table 1.3: CASA, KTLX and KOUN system characteristics.

RADAR	CASA	KOUN	KTLX
Frequency	9.41 GHz	2.7 GHz	3 GHz
Polarization: TX	Linear H and V	Linear H and V	Linear H
Polarization: RX	Linear H and V	Linear H and V	Linear H
Half Power Beamwidth (HPBW)	1.8°	0.93°	1°

Range Resolution	100 m	250 m	1 km
Maximum Range	30 km	313 km	460 km
Measured Variables	Z, Z_{dr}, Φ_{dp}, ρ_{hv}, LDR	Z, Z_{dr}, Φ_{dp}, ρ_{hv}	Z

iv. CP2

The CP2 radar is a unique dual wavelength system (S-band and X-band) with Doppler and polarimetric capabilities (at S-band) operating in Brisbane, Australia since August 2007. Two different datasets, corresponding to the thunderstorm season (in which substantial hail was detected), were analyzed: March 26, 2008 around 05:30 UTC and October 21, 2008 around 06:00 UTC. The CP2's X-band and S-band radars system characteristics are described in Table 1.4.

Table 1.4: CP2's X-band and S-band radar system characteristics.

RADAR	X-band	S-band
Frequency	9.4 GHz	2.8 GHz
Polarization: TX	Linear H	Linear H and V
Polarization: RX	Linear H and V	Co-polar to TX
Half Power Beamwidth (HPBW)	0.94°	0.93°
Range Resolution	150 m	150 m
Maximum Range	153 km	153 km
Measured Variables	Z, LDR	Z, Z_{dr}, Φ_{dp}, ρ_{hv}

v. Sounding

Two different sounding datasets were used here. One is from the local Norman, Oklahoma sounding from June 10, 2997 at 1200 UTC when analyzing CASA network data. The other one was constructed by knowing that the freezing level was located at 4 km and the -10°C located at 6 km. A lapse rate of 6.5° C km^{-1} was used below the melting level and 5°C above it.

C. Research Objectives

Can the wet ice attenuation component be corrected? Wet ice attenuation has been observed before at X and C bands. To be able to use X-band data in a precise way for quantitative estimation of precipitation, attenuation correction for wet ice needs to be taken into account. For this reason, two different correction methods were developed in this dissertation.

i. SRT Modified Method

The first correction method uses the S-band reflectivity as a reference to implement an *SRT*-modified technique where the α coefficient in the $A_h(X)$-$Z_h(X)$ power law relation is adjusted to meet the reference technique constraint.

ii. Piece-Wise Forward Method

Can the wet ice attenuation be estimated without using the un-attenuated reference signal? Given that a reference signal might not always be available, a second method was developed. This method uses a fixed $A_h(X)$-$Z_h(X)$ power law relationship to estimate the wet ice attenuation and corrects for it using the Hitschfeld-Bordan solution for attenuation correction in a forward methodology. To retrieve the location of the wet ice, an HID algorithm is used, providing the correction method with the starting range limit in the attenuation estimation.

CHAPTER II

II. BACKGROUND THEORY

A. Radar Theory Review

Radars are the primary tools used by weather forecasters for monitoring and prediction of severe and hazardous storms. Research related to technique and algorithm development primarily for tornado detection, flash floods and hurricanes has been on going now for several decades using the traditional single polarized Doppler radar. One of the main parameters extracted from radar measurements is the reflectivity (Z) measured in mm^6m^{-3} and typically expressed in dBZ ($10\log(Z)$). The reflectivity measured by the radar can be interpreted as a power measurement that describes the volumetric scattering from particles within a so-called resolution volume and given by the radar range equation as:

(1)

, where . This constant has the system characteristics of the radar included as well as of the particles in the resolution volume. The radar system parameters include the transmitted power P_t, the antenna gain G, horizontal and vertical beam widths θ and ϕ respectively, and finally the velocity of light c, pulse duration T_0 and wavelength of the signal λ. The particles within the volume are described by their dielectric factor , particle dimension (usually equivolume spherical diameter D) and number concentration N.

The reflectivity factor is defined from the drop size distribution *N(D)* as:

(2)

, where Z is in mm^6m^{-3} and D in mm. This definition is useful, especially when disdrometer data are available. It directly relates radar reflectivity measurements to the 6^{th} moment of the *N(D)*. The drop size distribution (DSD) or *N(D)* defines how many drops have diameters in the interval D to $D+\Delta D$ per unit volume. The DSD variability has been studied extensively for rainfall and many *Z-R* relations have been derived to estimate R given the radar measured Z. Probably one of the best known one is the exponential Marshall-Palmer distribution (Marshall and Palmer 1948)**:**

(3)

where the intercept N_o=8000 m^{-3} mm^{-1}, D is the drop diameter in mm and R is the rain rate in mm hr^{-1}.

With the advent of dual-linear polarized radars in the late 70's-early 80's, it is possible to extract more information on the particles and much research has been done and is still on-going to fully exploit the additional measurements made possible by dual-polarized radar systems. These radars have the ability to transmit and receive horizontally and vertically polarized signals. This results in the measurement of horizontal and vertical reflectivity, known as Z_h and Z_v respectively, as well as the complex correlation between the H and V signal returns. The advantage of using dual-polarized data is that substantial information can be extracted from the scanned volume as compared with single polarized Doppler radar. This information includes improved classification of 'meteo' vs 'non-meteo' echoes, and improved accuracy in the measure of R, hydrometeor type classification, etc, as described in detail by Bringi and Chandrasekar (2001) and references

therein. Dual-polarized weather radars are being actively pursued by the operational weather agencies in the US and Europe as well as other countries.

B. Radar signal interaction with hydrometeors

The fundamental description of the interaction of the incident radar beam and a particle is described by the so-called radar cross-section of the particle which expresses that portion of the incident power that is back scattered to the radar. This backscattered power is detected by the radar receiver. The single particle radar equation can be expressed as,

(4)

, where σ is the backscattering cross-section of the particle which depends on the size, shape and dielectric constant of the particle as well as the radar wavelength. If the target's size is small compared to the wavelength, the cross-section follows Rayleigh's approximation given by,

(5)

If the target's size is large compared to the signal's wavelength, the backscattering cross-section is just its geometrical area $\sigma = \pi a^2$, where a is the radius. On the other hand, when the target's size is comparable to the wavelength, the Mie approximation applies (see Bringi and Chandrasekar 2001 for more details). This presents an additional challenge but also provides a tool to detect hail in a storm by using two different frequencies.

Measuring the reflectivity at two different wavelengths provides extra information about the particles within the resolution volume. For a low frequency signal (e.g., 3 GHz) most precipitation particles scatter in the Rayleigh regime. For a higher frequency (e.g., 10 GHz), Mie

scattering effects may appear depending on the sizes of the particles within the resolution volume (e.g., hail larger than 1 cm). Differences in reflectivity measurements greater than about 3 dB can be attributed to Mie scattering and can be related in an approximate way to the particles' size. Raindrops can be as large as 8 mm without breaking apart, and for low frequencies (e.g., S-band) they satisfy Rayleigh scattering. However, when particles larger than about 10 mm exist (e.g., hail), they become Mie scatterers at the higher frequency (e.g., X-band) and a dual-frequency 'hail signal' can be defined as $HS=Z_h(S)-Z_h(X)$ (where both reflectivities are in dB, see Eccles 1975). This 'hail signal' can be as large as 20 dB (Battan et al. 1970; Eccles 1979; Tuttle and Rinehart 1983). While the Mie theory shows that for specific sizes and dielectric constants it can be negative as -4 dB, when a size distribution of hail exists, as is mostly the case, the *HS* is generally positive and reliable indicator of hail at the *HS* threshold of roughly 3 dB (Tuttle and Rinehart 1983). The latter reference also shows that negative hails signals can arise especially in regions of strong gradients due to inability to match the main beam and close-in side lobes at the two frequencies.

The Doppler weather radar makes use of the change in phase of the received signal from pulse to pulse to estimate the Doppler frequency shift. For the case of a dual-polarized radar (e.g., operating in the simultaneous transmit/receive mode), the H-polarized signal progressively lags the V-polarized signal due to propagation in a medium of oblate-spheroid oriented drops. In essence, the propagation constant at H-polarization differs to a small extent from that at V-polarization. Because of coherent scattering in the forward direction, the phase difference between the H and V polarized waves can become quite large and measureable as the propagation path increases. This phase lag is called differential propagation phase or simply differential phase.

(6)

, where Φ_{dp} is measured in degrees (°). It is more useful to define the change of differential phase over range than to use the differential phase itself. For a homogeneous path, it is known as the specific differential phase and is defined as,

(7)

, where K_{dp} is normally in units of degrees per kilometer (° km^{-1}). It is important to observe that these parameters (Φ_{dp} as well as K_{dp}) depend on the size, shape and orientation of the hydrometeors (Bringi and Chandrasekar 2001).

C. Radar signal attenuation and correction methods

When the radar's transmitted power travels through a medium it can experience attenuation, resulting in power loss of the signal due to scattering and energy absorption. The sampled volumes might be filled with gases, cloud particles, and/or precipitating particles. Depending on the wavelength, this attenuation might be significant or negligible. For example, attenuation due to gases is often negligible at frequencies below 10 GHz (Bean and Dutton 1968) and ice cloud particles attenuation is negligible too (Gunn and East 1954). On the other hand, radars with larger wavelengths, e.g. S-band radars at 10 cm, do not experience significant attenuation due to water or ice particles other than in extreme precipitation; while X-band radars operating at 3 cm experience significant attenuation due to rain. For this reason, varieties of algorithms have been developed and are available for rain attenuation correction at X-band.

For radars with single polarized reflectivity data, a method to correct for the attenuation was developed by Hitschfeld and Bordan in (1953) (*HB* method hereafter). The measured Z at range r (or, Z_m) is expressed in terms of the 'true' or corrected reflectivity (Z_c) and the path integrated attenuation *PIA* (where):

(8)

, where $k(s)$ is the specific attenuation factor (dB km^{-1}), A from now on. Assuming a power relation between A-Z as $A=\alpha Z^{\beta}$ where β is constant over range, the *HB* solution to equation 8 is

(9)

, where C is the calibration constant. Assuming that $Z_c(r=0)=Z_m(r=0)$, C becomes 1 and the *HB* solution is reached.

Having the *HB* method as a reference, the Surface Reference Technique (*SRT*) was developed by Meneghini et al. (1983). The *SRT* method was initially applied for airborne meteorological radars as a test-bed for space borne precipitation radar, e.g., TRMM (Iguchi et al. 2000). This method uses the radar cross section of the ocean surface as a reference to calculate the *PIA*. It compares the reflectivity measurements of the ocean surface in clear air with the measurements in the raining area. Any decrease in the measured surface cross section is attributed to the two-way attenuation along the propagation path.

A hybrid method using *SRT* and *HB* methods was developed by Iguchi and Meneghini in (1994). It compares the PIA_{SRT} with PIA_{HB}. When comparing the two, an α value (coefficient in the A-Z power law relationship) is chosen and adjusted until both values agree. This is called an α-adjustment method. When correcting by adjusting the α value it is assumed that any difference between the PIA_{SRT} and PIA_{HB} is due to the differences between the assumed and actual drop size distributions.

Other algorithms use the differential propagation phase Φ_{dp} (either directly or as a constraint; e.g., Bringi et al. 1990; Matrosov et al. 2002; Testud et al. 2000; Gorgucci et al. 1996; Park et al. 2005). A history of rain attenuation correction methods is well described in Park et al. (2005).

D. Attenuation due to wet ice

In events where rain is mixed with melting/wet ice (which frequently occurs in convective storms), an additional attenuation component appears making the total attenuation larger than that due to rain alone. Attenuation due to wet ice can be present at X and C band frequencies when these particles are as large as 1 cm (Battan 1971). Battan (1971) shows that melting ice around 2 cm in diameter with water shell thickness of 0.01 cm that are exponentially distributed, can produce two way attenuation as large as 6 dB km^{-1} at X-band and larger when the water thickness increases.

The Φ_{DP} based correction methods are not useful to correct for such type of attenuation. Wet ice (hail/graupel) does not have significant contribution on Φ_{dp} since these particles are nearly isotropic. This makes K_{DP} (change of Φ_{dp} over range) insensitive to isotropic scatterers. But even though wet ice does not contribute significantly to Φ_{dp} it does contribute significantly to the attenuation of the signal especially at higher values of reflectivity Z (typically over 45 dBZ).

While the attenuation due to the rain component of the mixture can be calculated using the *PIA* due to rain (based on Φ_{dp}), the attenuation due to the wet ice component is very difficult to estimate. In Battan (1971), the effect of water coating thickness variability in the wet ice specific attenuation estimation is shown. For example, a D_{max} of 2.9 cm and a water-shell thickness ranging from 0.01 cm to 0.1 cm gave a one-way attenuation between 3.4 to 4.0 dB km^{-1}**.** Here, an exponential drop size distribution derived empirically by Douglas (1964) was used. It is important to mention that the hail size distribution is difficult to measure. While on average, an exponential model might some describe hail showers, when the hail is melting, a gamma distribution was

found to be better (Fraile et al. 2003). Also, when the hail is large, a quasi-monodisperse distribution was found (Carte and Held 1978). This large variability in water coating thickness and the size distribution can give a variety of *A*-*Z* relations.

Despite of this, several relations have been established. For example, in Battan (1973) a *A*-*Z* was found for both X-band and S-band at T=0°C. Delrieu (1997) did the same for X-band at T=0°, 10° and 20°C. Rinehart and Tuttle (1984) established a $A_h(X)$-$Z_h(S)$ with radar data. Results are described in Table 2.1. Note that the units for *A* are dB km^{-1} while for *Z* it is mm^6 m^{-3}.

Table 2.1: *A*-*Z* relation coefficients found in different experiments.

Reference	α	β	Conditions
Battan (1973)	2.9×10^{-4}	0.72	X-band, T=0°C
	3.0×10^{-4}	0.62	S-band, T=0°C
Delrieu (1997)	9.8×10^{-5}	0.76	X-band, T=0°C
	1.0×10^{-4}	0.8	X-band, T=10°C
	1.0×10^{-4}	0.83	X-band, T=20°C
Rinehart and Tuttle (1984)	4.8×10^{-4}	0.60	$A_h(X)$-$Z_h(S)$

CHAPTER III

III. WET ICE ATTENUATION CORRECTION WITH SRT MODIFIED METHOD

In Liu et al. (2006a), a technique was proposed to correct for both rain and wet ice attenuation as well as to separately estimate the attenuation due to each component. A RAMS model supercell simulation using the one moment scheme (van den Heever and Cotton 2005), described by Huang et al. (2005), was used to simulate X-band and S-band dual-polarized radar RHI scans. Here, a RAMS model supercell simulation data using the 2 moment scheme (as described by Meyers et al. 1997) is used to simulate dual-polarized X-band and NEXRAD H-polarized radar data.

If only rain exists along the propagation path, a simple attenuation correction method is used (Bringi and Chandrasekar 2001), where for an inhomogeneous path,

(10)

With this, the attenuated reflectivity can be related to the un-attenuated one and the path integrated attenuation (*PIA)* quantified along the beam. By knowing the specific attenuation and , the attenuation due to rain can be corrected by simply using,

(11)

Since it is known that any Φ_{dp} based correction method will correct only for rain induced attenuation, we can calculate the *PIA* as well as A_h as a function of range along the path just for rain.

To make the correction due to wet ice at X-band, a non-attenuating wavelength (e.g., S-band) radar reference signal can be useful (but not necessarily the entire range profile). The S-band radar needs only to provide the (un-attenuated) reflectivity value at the maximum range of the X-band beam. This is used as a reference to calculate the dual wavelength ratio (*DWR*) at the end of the path (from now on ΔZ). Note that ΔZ is the difference between the un-attenuated S-band reflectivity and the rain-corrected X-band reflectivity at the end of the beam. In practice, the S-band and X-band radars will not be collocated and some space/time interpolation will be needed. The TRMM Surface Reflection Technique (*SRT*) α-adjustment method (Iguchi et al. 2000) is used to apportion the ΔZ backwards along the beam. The *SRT* uses an initial power law for rain and it adjusts the coefficient α (assuming that β is fixed). The β value may vary depending on the wet ice mean size but it is fixed here to 0.6 considering that the values (from Tuttle and Rinehart 1983) varied from 0.456 and 0.648 (above and below melting layer, respectively). The initial value of α was set to 0.00048 as in Tuttle and Rinehart (1983). This α is adjusted such that $\alpha_{adj}=\alpha\varepsilon$ matches the ΔZ in ε, where ε is the attenuation correction factor defined by Iguchi et al. (2000) as,

(12)

In this last equation the denominator is defined as,

(13)

, where , $r_1=0$, $r_2=R_{max}$, and Z_m is the measured X-band reflectivity in units of $mm^6\,m^{-3}$ (in our case we assume Z_m is the one that was already corrected for rain attenuation using equation 11).

If the defined correction factor in equation 12 as a function of α_{adj} (assumed to be constant along the propagation path), the corrected reflectivity at X-band due to wet ice only can be calculated by,

(14)

A flow diagram of this algorithm is shown in Figure 3.1 of what we call the *SRT*-modified method.

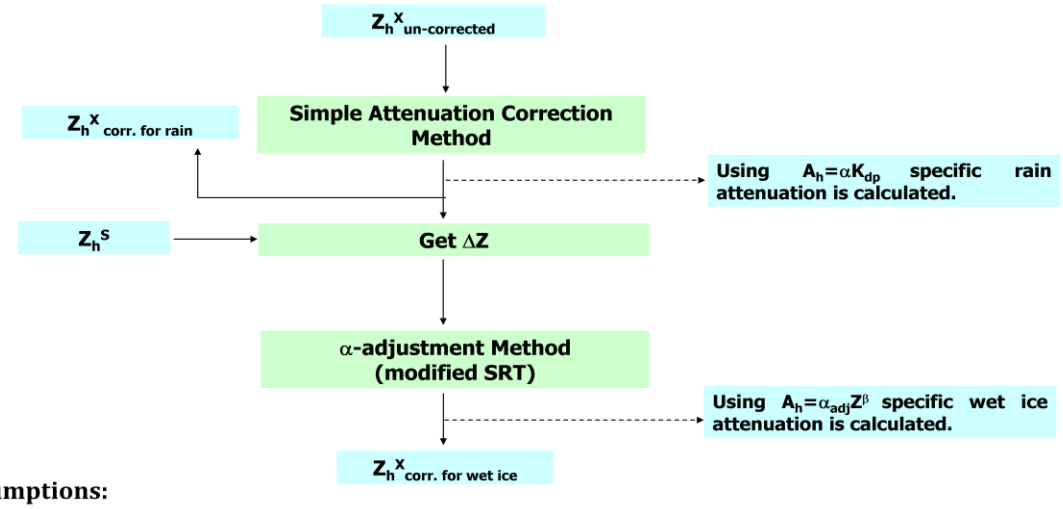

Assumptions:

- While correcting the X-band reflectivity Z_h^X we assume that we have available Z_h^S at the end of the beam.
- In the simple attenuation correction method we are assuming α=0.25 dB/° for rain
- In the α-adjustment method we are assuming a fixed β=0.6 and an initial α=0.00045 dB/°

Figure 3.1: Wet ice attenuation correction using *SRT*-modified method.

A. RAMS

Using the radar emulator results from the RAMS model supercell simulation, variables like reflectivity, specific attenuation and specific differential phase were computed. Figure 3.2 shows gridded data of intrinsic reflectivity along with contours of specific attenuation of rain and wet ice.

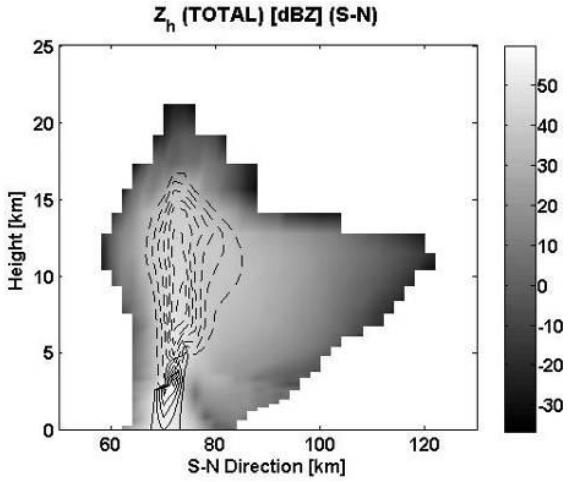

Figure 3.2: True specific attenuation contours of rain (solid line) and hail (dashed line) over true X-band reflectivity (background) on the S-N Direction cross-section (RHI scan) using the RAMS model.

The path integrated attenuation *PIA* was calculated by integrating the specific attenuation A_h provided by the RAMS model's microphysics. The results are shown in Figure 3.3, where the total *PIA* (rain + wet ice), the *PIA* due to rain, and the *PIA* due to wet ice have maxima of 45, 18 and 25 dB, respectively.

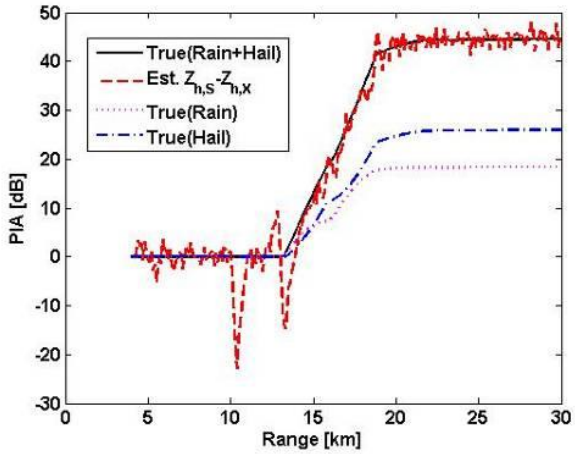

Figure 3.3: Path integrated attenuations (*PIA*) at 12.6° in elevation for total (rain + wet ice), rain and wet ice.

These values are derived from the true specific attenuation. Also shown is the dual-wavelength ratio, e.g., $Z_h(S)$-$Z_h(X)$ with Gaussian measurement noise added (σ = 1 dB at each frequency). Note that $Z_h(X)$ is attenuated by all hydrometeors along the path. In the same way, Gaussian noise with σ = 2° was added to the specific differential phase K_{dp} that was used to retrieve the differential phase Φ_{dp} at X-band. This Φ_{dp} was used to correct the rain induced attenuation using the simple attenuation correction method as described in equation 11. Figure 3.4 shows a typical correction for a radar beam at 2° elevation angle that just contains rain. As can be seen, the simple attenuation correction method works well for rain only and compares well with the $Z_h(S)$.

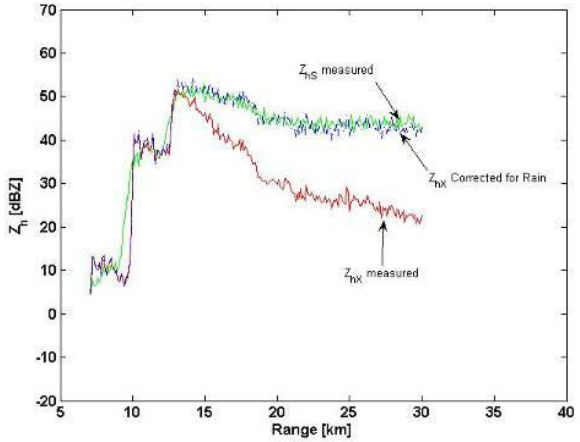

Figure 3.4: Rain attenuation correction of the X-band signal using RAMS model data. This radar beam is at 2° in elevation and only rain is present along the propagation path.

On the other hand, when this method is applied to a radar beam containing rain mixed with wet ice, this correction method based on Φ_{dp} is not enough (see Figure 3.5). As expected from the *PIA* calculations, the rain attenuation is about 18 dB. This is the amount corrected by the simple attenuation correction method. We can observe that the signal is still attenuated because of the wet ice component that is not affected by the Φ_{dp} based method, thus affecting the signal up to 25 dB.

To correct for this additional attenuation, the proposed α-adjustment method was used where the S-band (un-attenuated) *Z* at the maximum range of the beam is used as a reference to get the ΔZ which is 28.9 dB in this case. This way the $Z_h(X)$ profile, that was just corrected for rain, is retrieved using the variant of the *SRT* method described earlier in equation 13. Figure 3.5 shows the $Z_h(X)$ corrected for both rain and wet ice compared to the un-attenuated $Z_h(S)$. Comparing the intrinsic *PIA* due to wet ice in Figure 3.3 (25 dB at the maximum range of the beam) with the ΔZ in Figure 5 (28.9 dB) we can notice the consistency between them to within several dB. Notice that if we compare the S-band *Z* and the X-band corrected one in Figure 3.5; they are within a few dB along the entire beam (by visual inspection).

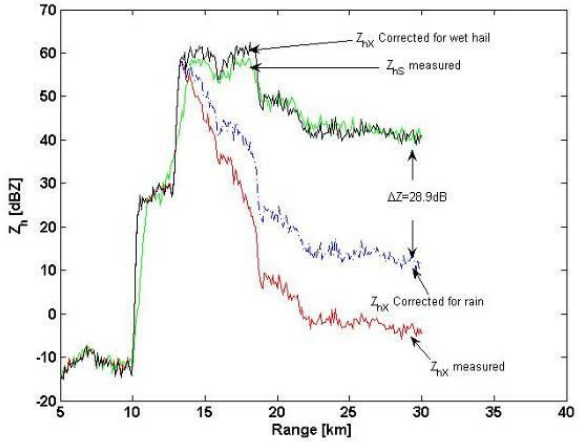

Figure 3.5: Rain and wet ice attenuation correction of the X-band signal using RAMS model data. The radar beam is at 12.6° in elevation.

The retrieval procedure for obtaining the vertical structure of the specific attenuation is based on the simulated RHI scan beams. The contours of the specific attenuation due to rain are shown in Figure 3.6 and the ones due to wet ice are shown in Figure 3.7.

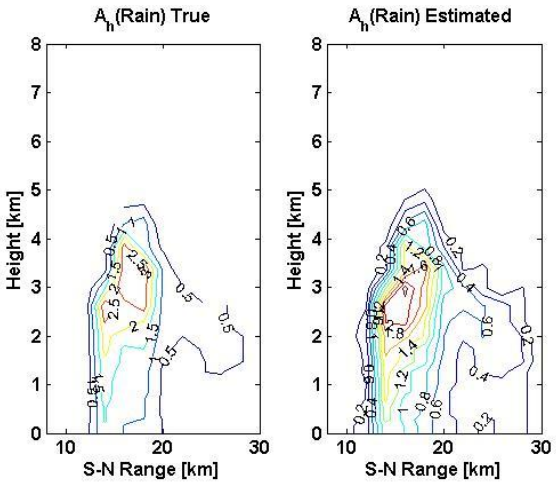

Figure 3.6: Rain specific attenuation $A_h(X)$ vertical cross-section retrieval for the S-N direction for an RHI scan.

These vertical sections of the specific attenuation $A_h(X)$ are from the core of the storm where the maximum $Z_h(S)$ is detected. In each figure the left panel plots shows the intrinsic specific

attenuation from RAMS microphysical outputs while the right panel plots show the simulated radar-based retrievals. Both specific attenuations due to rain have maxima of 2.5 dB km^{-1}. Observe that the both panels are plotted with a step of 0.5 dB km^{-1}.

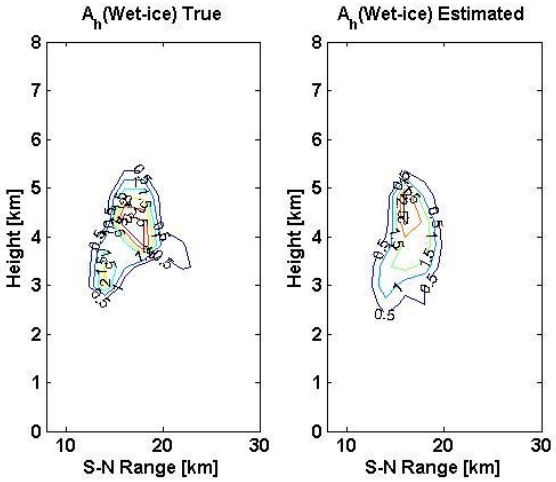

Figure 3.7: Wet ice induced specific attenuation $A_h(X)$ vertical cross-section retrieval for the S-N direction for an RHI scan.

To quantify the error, by comparing with true values, in Figure 3.6, the peak attenuation due to rain is well estimated with 0.4 dB km^{-1} maximum RMS error from the intrinsic values. The same 0.20 dB km^{-1} maximum RMS error from its intrinsic values was found in the wet ice case shown in Figure 3.7 where both specific attenuations values have maxima of 2.5 dB km^{-1}.

B. IHOP: June 16th, 2002

The XPOL radar is described in Anagnostou et al. (2004). The SPOL radar was operated by the National Center for Atmospheric Research (NCAR). These two radars were in close proximity to each other. The beams from the two radars were 'matched' by Anagnostou (personal communication) and matched data were provided to us. The *SRT*-modified method for estimating and correct the wet ice specific attenuation at X-band separate from rain was followed using the XPOL/SPOL radar data (see Figure 3.8).

Figure 3.8 shows a range profile at 2º elevation angle depicting the X-band Z_h correction for both rain and wet ice. In this profile the ΔZ = 9 dB at the end of the propagation path. It is shown that the correction is good if we compare the attenuation-corrected $Z_h(X)$ with the un-attenuated $Z_h(S)$ in spite of the beams not being exactly matched in range resolution and sampling time.

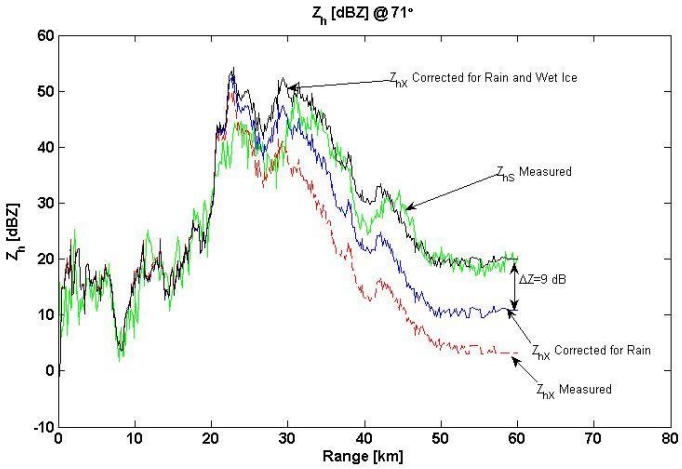

Figure 3.8: Rain and wet ice attenuation correction of the X-band signal using the XPOL and SPOL data. A PPI scan at 2° in elevation and 71° in azimuth was used.

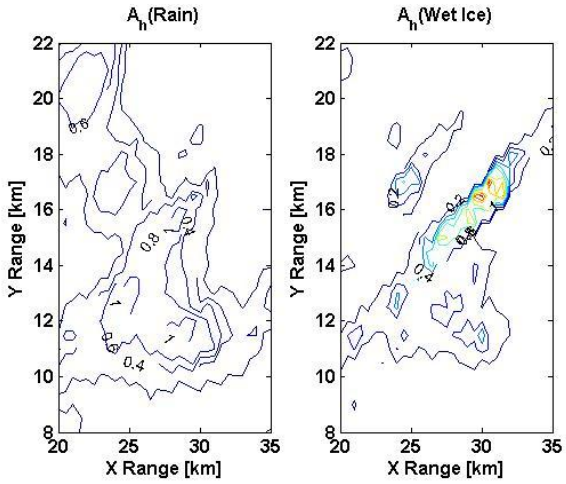

Figure 3.9: Rain (left panel) and wet ice (right panel) attenuation retrieval using the XPOL and SPOL data.

Figure 3.9 shows the contours of the specific attenuation for rain (left panel) and wet ice (right panel). These are estimated from the XPOL/SPOL from the PPI scan data set at 2º elevation

angle. The $A_h(X)$ maxima due to rain is 1 dB km^{-1} and the one due to wet ice is approximately 1.2 dB km^{-1}. In this plot the steps are 0.2 dB km^{-1}. As shown in Figure 3.10, the results look 'reasonable' when overlaid with the corrected $Z_h(X)$.

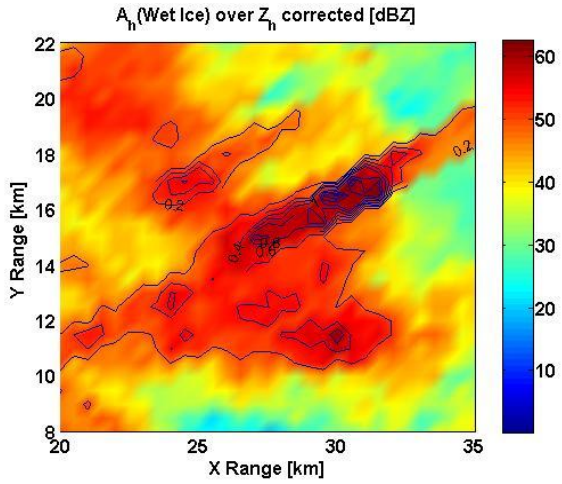

Figure 3.10: Wet ice specific attenuation contours overlaid with corrected $Z_h(X)$ PPI scan at 2° in elevation.

C. CASA

Two different datasets were considered; a stratiform event and a convective event. A cross-radar Z bias was found and corrected for using data from the stratiform event of June 20, 2007. This is of great importance for obtaining reliable results.

i. CASA/KTLX: June 20, 2007; Stratiform Event (CASA07A)

For the stratiform rain event, little or no attenuation was observed as expected. Figure 3.11 shows a ray extracted from 2° in elevation PPI scan at 113° in azimuth.

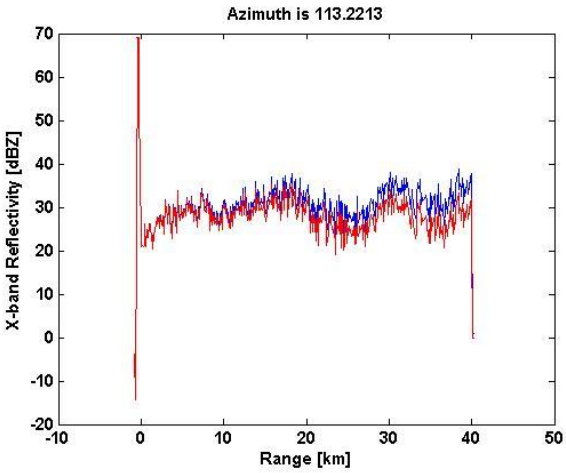

Figure 3.11: CASA Rush Springs RSP radar data for stratiform event at 2° in elevation and 113° in azimuth. The red is the un-corrected reflectivity and the blue line is corrected for rain.

When using the S-band value at the end of the beam it is found that the ΔZ of 0.13 dB. This is expected since the combination of little attenuation with the reflectivity differences due to the frequency differences (Mie effect) should not be more than 3 to 5 dB.

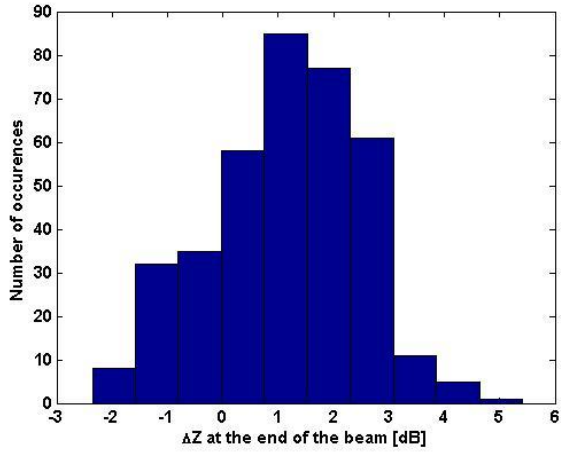

Figure 3.12: ΔZ histogram of the whole dataset showing the number of occurrences.

When the whole scan was evaluated via a histogram, shown in Figure 3.12, shows ΔZ differences up to 2 dB and concentrated around 1 to 2 dB. S-band data from KTLX was used as comparison.

The histogram shows that, in the case of stratiform rain, the differences in X-band and S-band reflectivity for the CASA and NEXRAD (KTLX) radars are within the expected errors.

ii. CASA/KOUN: June 10, 2007; Convective Event (CASA07B)

The hydrometeor classification (HID) algorithm (at S-band) showing the presence of wet (high density) graupel is shown in Figure 3.13. This figure shows a constant altitude PPI (CAPPI) at 6.5 km. The location of wet ice attenuation should contribute to the excess attenuation of the X-band signal.

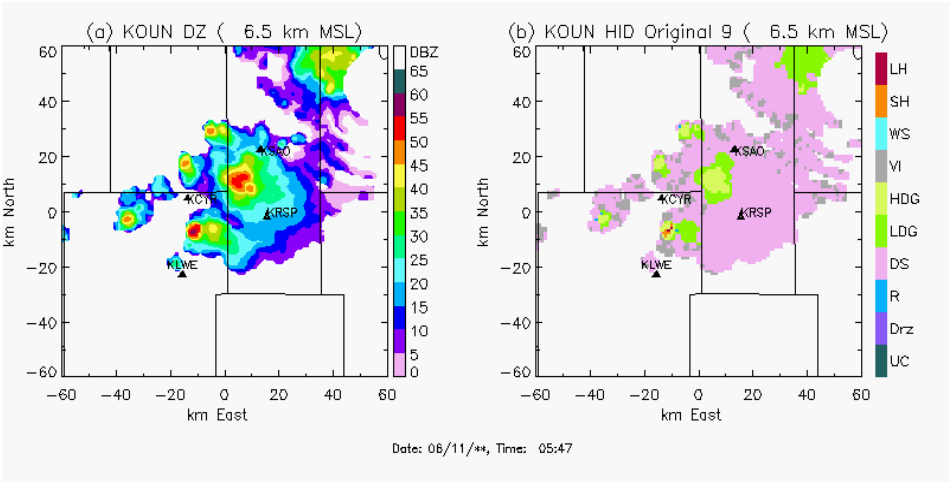

Figure 3.13: S-band, KOUN, Hydrometeor Classification (provided by Brenda Dolan). Left panel is a CAPPI of reflectivity. Right panel is the Hydrometeor Classification (HID) both at 6.5 km.

When examining this case (Figure 3.14) there were other thresholds taken into consideration, different than other datasets analyzed. A signal-to-noise ratio (*SNR*) filter at the end of the beam was applied to make sure that the values were not reaching the noise level. High attenuation due to rain or wet ice can make the signal to go below noise or even be lost completely. Therefore a *SNR* constraint of 5 dB was applied.

When the X-band value at the maximum range of the beam was obtained, it's location in latitude/longitude/height served as reference to find the corresponding S-band value. Then an average of the $Z_h(S)$ surrounding gates around the X-band gate was performed in order to get a reliable value. To calculate the ΔZ and apply the wet ice correction method, the rain corrected $Z_h(S)$ of from the CASA radars was used. Specifically the Cyril (CYR) radar data for the CASA07B is shown herein.

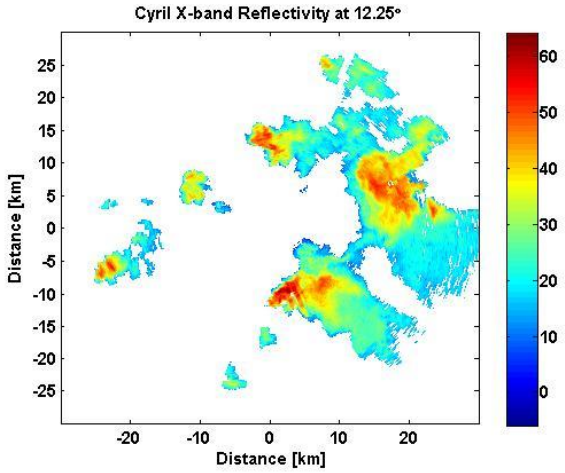

Figure 3.14: CASA Cyril CYR $Z_h(X)$ corrected for rain. PPI scan at 12.25° in elevation.

Figure 3.15 shows the reflectivity beam going through the high density graupel region. The blue line is the $Z_h(X)$ range profile corrected for rain, while the green line shows the corrected range profile for wet ice (e.g., total attenuation correction).

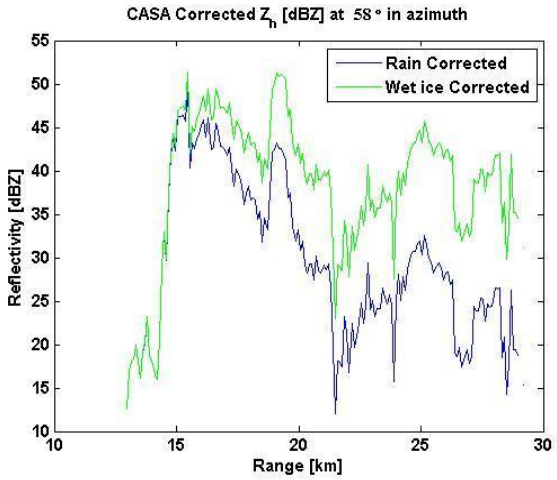

Figure 3.15: CASA Cyril CYR $Z_h(X)$ corrected for rain (blue) and for wet ice (green) along the propagation path at 12.25° in elevation and 58° in azimuth.

The wet ice attenuation correction was done after obtaining a ΔZ of 16 dB at the maximum range of this beam. When the whole data set was corrected, the wet ice attenuation was estimated using the *SRT*-modified technique. The attenuation due to wet ice, which is overlaid with reflectivity shown in Figure 3.16, shows to have maxima of 5 dB km^{-1}. The retrieved specific attenuation shows good agreement with values of Z in wet ice regions where values are expected to be over 55 dBZ.

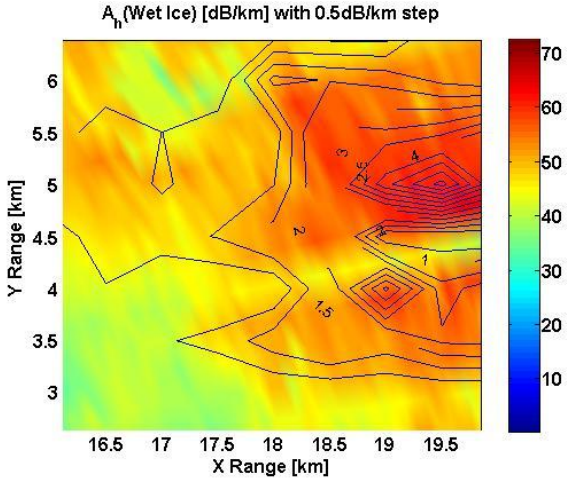

Figure 3.16: Contours of specific attenuation $A_h(X)$ due to wet ice overlaid with wet ice corrected

$Z_h(X)$.

D. CP2 Radar

i. March 26th, 2008 Event (CP208A)

For this event strong attenuation was observed in the X-band signal in comparison with the S-band one (see Figure 3.17). For this data set, no rain attenuation correction was provided, so a simple attenuation correction as described in equation 11 was used.

To apply the Φ_{dp} attenuation correction method, the $K_{dp}(S)$ provided by the polarimetric S-band radar was used in an empirical relation obtained from DSD data in order to get $A_h(X)$ due to rain (described in equation 14).

$$A_h(X)^{rain} = 0.0917\,(K_{dp}^{S})^2 + 0.6454\,K_{dp}^{S} + 0.1749 \tag{14}$$

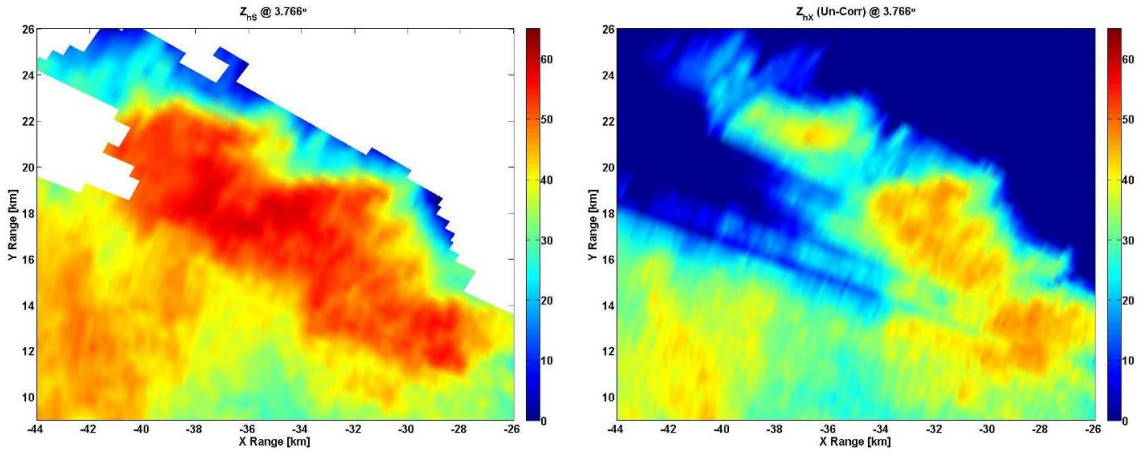

Figure 3.17: The left panel plot shows the $Z_h(S)$ PPI at 3.766° in elevation. In the right one is shown the $Z_h(X)$ PPI measured at the same elevation. It is clearly noticed the attenuation of the X-band signal.

Figure 3.18 shows the reflectivity profiles with and without corrections at 3.7° in elevation. As seen in this figure, the Φ_{dp} based attenuation correction method, only corrected the rain

attenuation component of the total attenuation. A ΔZ of 34.77 dB was found at the end of the beam and was used to correct the remaining wet ice induced attenuation. The corrected $Z_h(X)$ is comparable with the $Z_h(S)$.

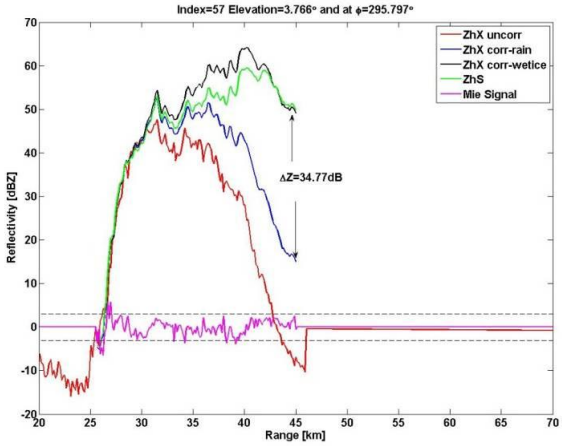

Figure 3.18: $Z_h(X)$ range profiles with rain and wet ice corrections applied for a ray at 3.7° in elevation. A ΔZ of 34.77dB was observed. No 'Mie signal' is present.

By inspecting the contours of the rain specific attenuation over the $Z_h(X)$ PPI scan (Figure 3.19), a maximum attenuation of 2.5 dB km^{-1} is observed. In the case of the wet ice, the maximum specific attenuation retrieved is 3.5 dB km^{-1} (Figure 3.20) in the highest corrected reflectivity area.

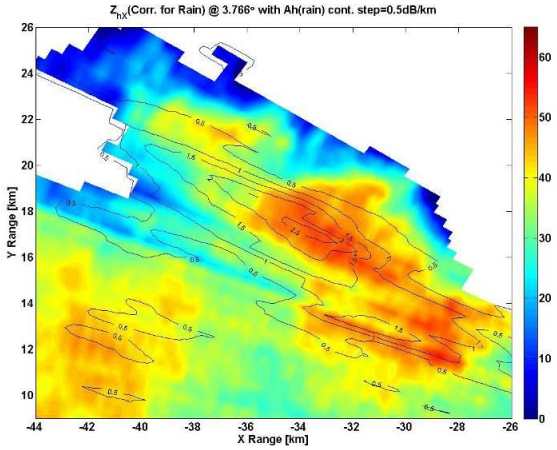

Figure 3.19: $Z_h(X)$ corrected for rain with specific attenuation $A_h(X)^{rain}$ contours overlaid.

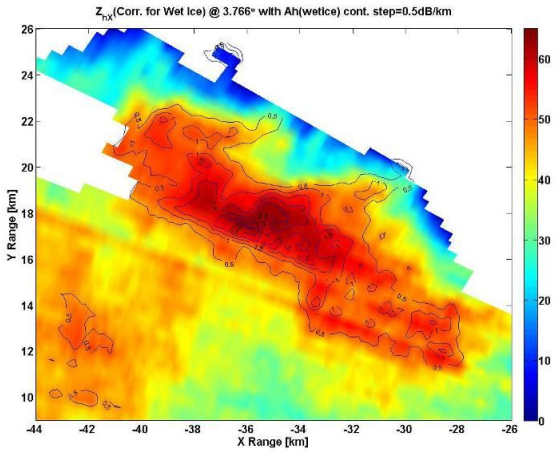

Figure 3.20: $Z_h(X)$ corrected for wet ice with retrieved specific attenuation $A_h(X)^{wet\ ice}$ contours overlaid.

When this 'corrected for wet ice' reflectivity in Figure 3.20 is compared to the reflectivity at S-band in Figure 3.17 the correction shows good agreement. Also notice the comparison of the reflectivity corrected for rain only (Figure 3.19). The $Z_h(X)$ corrected for rain is still attenuated. The proposed correction method took care of that extra attenuation not corrected by the Φ_{dp} based method.

ii. October 21, 2008 Event (CP208B)

In the October event a convective hail storm was observed with the CP2 radar. In Figure 3.21 (left panel plot) the $Z_h(S)$ showed reflectivities as high as 65 dBZ. When looking into the corresponding X-band PPI (Fig 3.21 right panel), attenuation is evident in these high reflectivities areas. The features shown in the right plot cannot even be noticed in the left one. Note that these PPIs are at 2.4° in elevation.

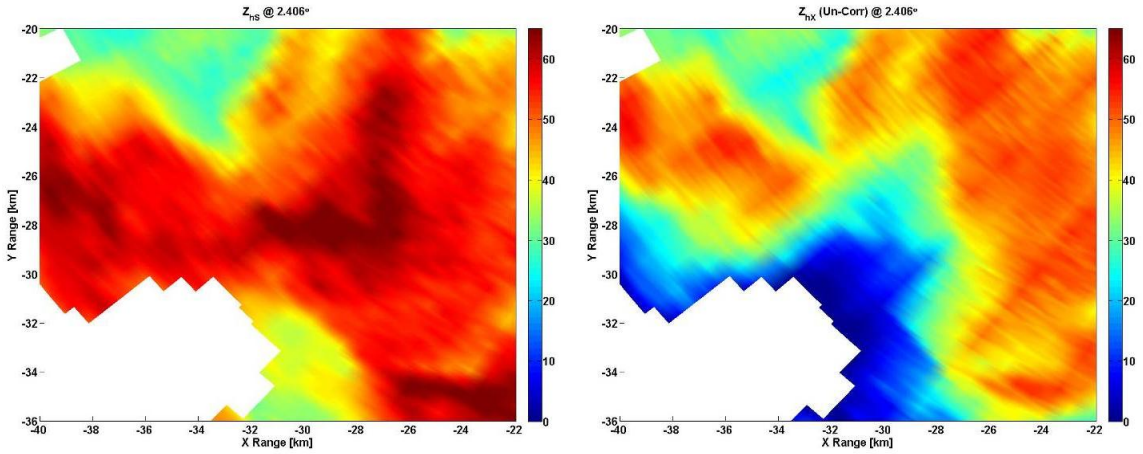

Figure 3.21: The left panel plot shows a reflectivity $Z_h(S)$ PPI measured at 2.4°. In the right one is shown the $Z_h(X)$ PPI at the same elevation. It is clearly noticed the attenuation of the X-band signal.

A radar beam passing through one of these areas was chosen. Figure 3.23 shows the $Z_h(X)$ reflectivity profile where a maximum of $Z_h(S)$ of 65 dBZ is detected. By comparing to the S-band reflectivity profile, the rain correction method shows again that is not enough to get a completely corrected profile. As a ΔZ of 17.33 dB is observed at the end of the beams the proposed wet ice correction method was applied.

While doing this process it was observed that there was a Mie effect in the X-band signal that was affecting the correction. The 'Mie signal' was obtained following equation 15.

$$Mie\ Signal = DWR - DWR^{f} \quad (15)$$

By filtering the dual wavelength ratio (defined as $DWR=Z_h(S)-Z_h(X)$) and taking the difference with the non-filtered one, reflectivity differences effect due to Mie scatterers are detected. Only differences over 3 dB were considered following Tutlle and Rineheart (1983) where Mie signals between -3 to 3 dB were ignored to avoid the noisiness of the hail signal. This then is removed from the measured X-band reflectivity. When this is done before any attenuation correction method, the resulting corrected signal does not show over correction. In Figure 3.22 a 'Mie signal' of 10 dB is observed. If this 10 dB is not removed from the measured $Z_h(X)$ these 10 dB are reflected in the final corrected profile as an overcorrection in this area. Because it was considered, the resultant $Z_h(X)$ corrected for wet ice shows to follow the $Z_h(S)$ that is assumed to be un-attenuated.

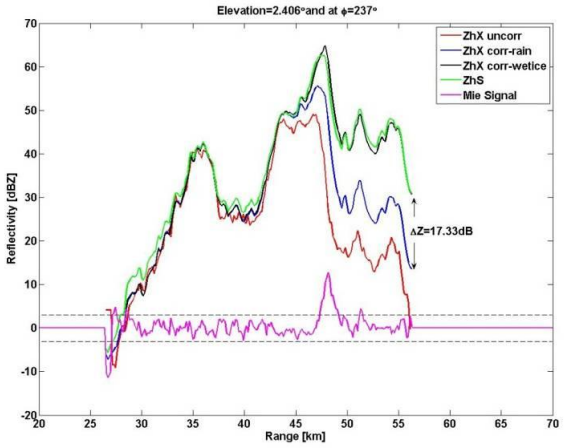

Figure 3.22: $Z_h(X)$ range profiles with corrections applied. The Mie 'hail' signal is included.

The retrieved specific attenuation is plotted as contours over $Z_h(X)$ corrected for rain in Figure 3.23. This 'rain corrected' PPI still does not show the high reflectivity features of the S-band PPI. As the proposed wet ice correction method is applied, these high reflectivity features show up (Figure 3.24). In this same figure the retrieved $A_h(X)^{wet\ ice}$ contours are shown and have values up to 5 dB km^{-1}.

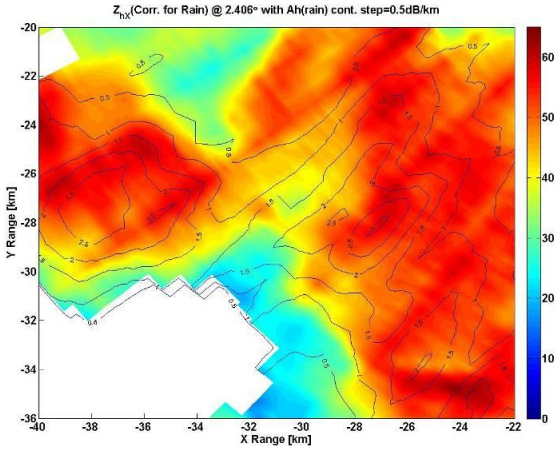

Figure 3.23: $Z_h(X)$ corrected for rain with retrieved specific attenuation $A_h(X)^{rain}$ contours overlaid.

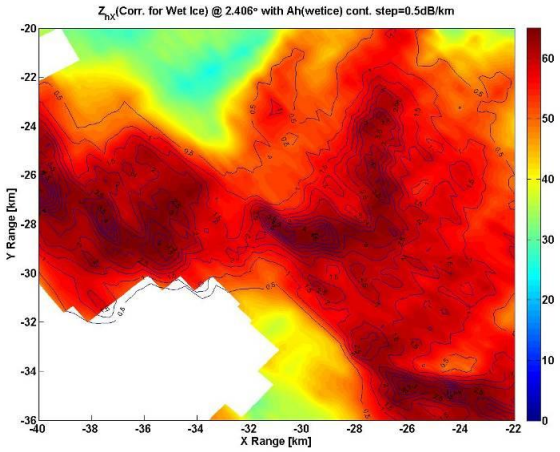

Figure 3.24: $Z_h(X)$ corrected for wet ice with retrieved specific attenuation $A_h(X)^{wet\ ice}$ contours overlaid.

To judge how accurate the correction methodology is, the differences between the assumed un-attenuated $Z_h(S)$ and wet ice corrected reflectivity $Z_h(X)$ *as* $\Delta Z = Z_h(S) - Z_h(X)^{corrected}$ for the whole data set are plotted as a histogram in Figure 3.25. Most of the occurrences are concentrated over zero but there are still some ΔZ out of the expected bounds of $-2 \leq \Delta Z \leq 4$ dB. A mean of 0.41 and standard deviation of 1.2 were found indicating that the results were inside the reasonable bounds.

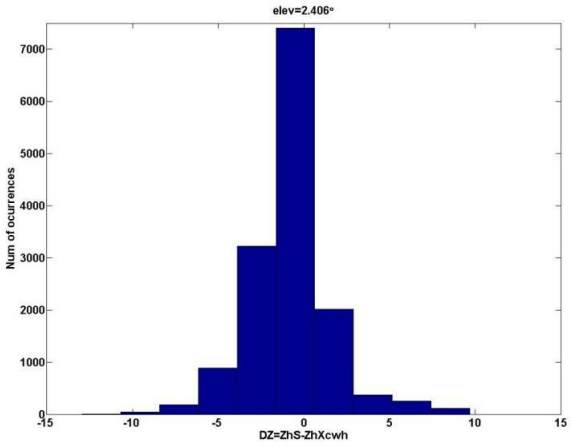

Figure 3.25: ΔZ histogram for the whole dataset showing the number of occurrences. This ΔZ is the difference between the $Z_h(S)$ and the $Z_h(X)$ corrected for rain and wet ice along the whole beam (not just at the end).

CHAPTER IV

IV. WET ICE ATTENUATION CORRECTION USING PIECE WISE FORWARD METHOD

A new technique to estimate and correct for wet ice specific attenuation was developed as an attempt to eliminate the un-attenuated (S-band) reference used in the previous section. It is needed to emphasize that a collocated reference signal or a reference of any type might not always be available, limiting the correction method described in Chapter III. Therefore an attenuation correction method that does not depend on such a reference is needed.

Different than the method described in Chapter III, an α adjustment is not used in this correction method. Instead, an $A_h(X)^{wet\ ice}$-$Z_h(X)$ relation is established, where the α and β values are fixed. Data from the CP2 radar from the CP208A event were used to retrieve these values. This method has two purposes. One purpose is to still be able to estimate the wet ice specific attenuation $A_h(X)^{wet\ ice}$ separate from that of rain, and the other purpose is to use this estimation to perform the correction.

Once the $A_h(X)^{wet\ ice}$-$Z_h(X)$ power law relation coefficient values are found, they are used in the Hitschfeld-Bordan solution for the specific attenuation due to wet ice defined as,

(15)

With defined in equation 13, the specific attenuation is calculated and used to correct in a forward way using,

(16)

Also, different from the method described in Chapter III, the integration limits used in are defined in a different way.

First, the HID algorithm described in Dolan and Rutledge (2009) is used to identify where the wet ice is located. This algorithm identifies high density graupel. Here high density graupel is inferred to include hail because both are assumed to attenuate the signal due to absorption. The latter can occur when graupel or hail melts as it falls below the 0°C level or when hail is in wet growth above the 0°C level. This fuzzy-logic based algorithm makes use of the polarimetric variables such as Z_h , Z_{dr}, K_{dp} and ρ_{hv}, along with temperature profiles to distinguish between seven different classes. These classes include drizzle, rain, aggregates, pristine ice crystals, low density graupel, high density graupel and vertical ice. The HID algorithm was tested for both S and X bands simulated and real data showing confident results.

When applying the HID algorithm, the location of high density graupel is identified. If five consecutive range gates (around 750 m) are identified as having wet ice, then the first gate will be defined as r_1. When the radar signal travels through an attenuating medium (such as rain and/or wet ice), the path integrated attenuation increases until the end of the storm. For this reason, if wet ice is along this path then it will degrade the signal up to $r_2=R_{max}$. Then the attenuation due to wet ice calculated with equation 15 just includes the area affected by the wet ice and not the rain (which is assumed was already corrected for). This is why this method is named Piece-Wise Forward *(PWF)*, because it just corrects for the degradation of the signal in that area only.

Is important to mention that this method was developed for X-band polarimetric radars with the ability to measure polarimetric variables such as Z_{dr}, K_{dp} and ρ_{hv}, in addition to the reflectivity Z_h. The CP2 radar (from which datasets were used to test and demonstrate the results of this method)

does not have the ability to measure these variables at X-band but can measure them at S-band. Because of this, the HID algorithm was implemented using S-band measurements and then the results were used to correct the X-band ones. This introduces a question of whether identifying that first gate (considering that it is threshold to 5 consecutive range gates with a positive identification for wet ice) in X-band will be accurate. The attenuation of the X-band signal due to the wet ice in the first 5 to 10 gates is not as significant as in further range gates (as shown in all the profile plots presented here). Attenuation in these first gates, where the wet ice core is first detected, will not attenuate the $Z_h(X)$ more than 2 dB. This will not make a considerable difference in identifying where radar signal first meet the mixed phase region and might miss by one or two gates. Therefore this should not be a big concern.

Drawback and other challenges will be described with examples when discussing the results.

A. A-Z RELATION COEFFICIENTS RETRIEVAL

To be able to estimate the wet ice specific attenuation, the coefficients of the $A_h(X)^{wet\ ice}$ - $Z_h(X)$ power law must be established. Table 2.1 shows the α and β coefficients found for this relation by analyzing different datasets under different conditions. These values are used as reference when analyzing the datasets available for this research.

For the $A_h(X)^{wet\ ice}$ retrieval the *DWR* from the CP208A event was used (Bringi et al. 2009). The *DWR* is used to estimate the total specific attenuation and the rain component is estimated using $K_{dp}(S)$ as described in equation 14. Then $A_h(X)^{wet\ ice} = A_h(X)^{TOTAL} - A_h(X)^{rain}$. Using this procedure the wet ice specific attenuation is retrieved to further relate to $Z_h(S)$. In Table 4.1, the coefficients found from these different datasets are displayed along with which data set was used and the conditions. Although the results found in the literature review are developed under certain conditions, thresholds were applied to try to emulate these. For example, a hail detection ratio

(*HDR*) (Aydin et al. 1986) threshold of higher or equal to 10 dB was applied to ensure that hail was present. Also, only values for $Z_h(S) \geq$ 35 dB were used in the relation retrieval.

Additional to these coefficients, the coefficients for the same relation in a rain environment were examined, were found to be similar with what has been found in the literature review.

Table 4.1: A_h-Z_h power law relation coefficient and exponent found in different datasets. CP2 measurements correspond to the CP208A event analyzed here, and the Brisbane 2DVD disdrometer data were used for simulations.

REFERENCE	α	β	Conditions
From CP2 Measurements	7.0×10^{-4}	0.5529	$Z_h(S)\geq$35dBZ, HDR≥10dB, Hail below melting layer
From Brisbane Disdrometer Simulations	1.9038×10^{-4}	0.7085	$A_h(X)$-$Z_h(X)$, T=0°C

In Appendix A, a vertical cut at 297° of $Z_{dr}(S)$ was constructed out of PPI scans with elevations ranging from 0.44° to 16°. The plot shows some α and β values found for $A_h(X)$-$Z_h(S)$ depending on the area examined for these datasets. These coefficients were retrieved under different conditions to that described in Table 4.1 but serve as reference to the ones retrieved for the *PWF* correction method. Also, the $Z_{dr}(S)$ shows that the mixed phase region is located around 40 km from the radar and the local decrease in $Z_{dr}(S)$ shows a hail shaft.

B. CP208A Event

Examining the relations retrieved from two different datasets (Table 4.1), β=0.5529 and $\alpha=7\times10^{-4}$ were used to estimate the specific attenuation due to wet ice at X-band and correct for it. It has to be mentioned that these coefficients were found using $Z_h(S)$ and not $Z_h(X)$, but from other dataset analysis, there was not a significant difference between the coefficients in both frequencies in the

absence of Mie scattering. Considering that the CP2 does not have a corrected reflectivity at X-band, the un-attenuated $Z_h(S)$ was used instead. However, the radar data simulated from the disdrometer data, does have an un-attenuated X-band reflectivity which was used to retrieve the coefficients shown in Table 4.1.

Figure 4.1 shows the S-band reflectivity PPI measured from the CP2 radar. Having this data is useful when comparing the results from the *PWF* correction method, since we are assuming that the S-band reflectivity is not attenuated. High attenuation is observed when comparing the S-band (left plot) to the uncorrected X-band (right plot) reflectivity in Figure 4.1.

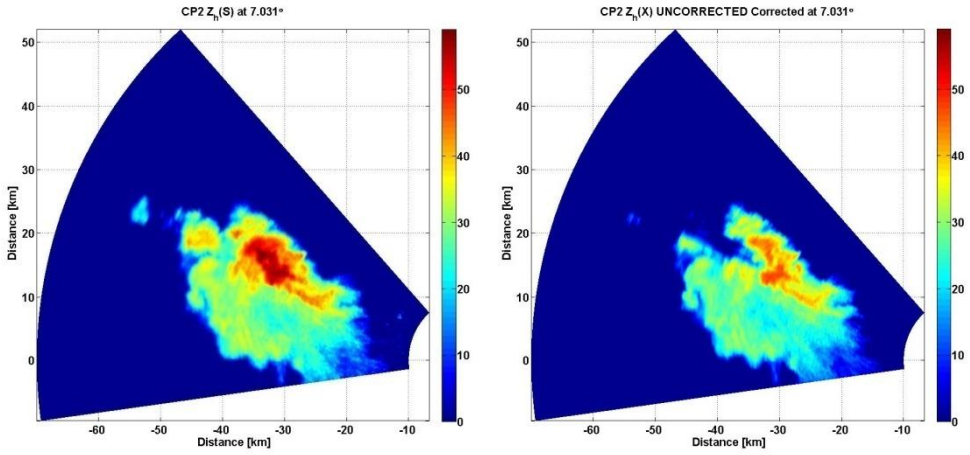

Figure 4.1: The left panel plot shows the $Z_h(S)$ PPI at 7° in elevation. In the right one is shown the $Z_h(X)$ PPI measured at the same elevation. The attenuation of the X-band signal is clearly observed.

As a first approach to correct for the induced attenuation, the rain specific attenuation is estimated and corrected using the same $A_h(X)^{rain}$-$K_{dp}(S)$ relationship as described in equation 14. Results are shown in Figure 4.2. If compared with the $Z_h(S)$ in the left panel of Figure 4.1, it is clearly observed that additional attenuation is affecting the measurements of reflectivity since higher reflectivity core is not identified.

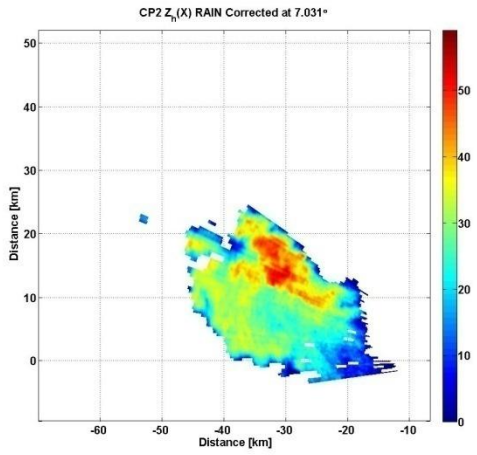

Figure 4.2: $Z_h(X)$ PPI corrected for rain at 7° in elevation. If compared with $Z_h(S)$ in the left panel of Figure 4.1, attenuation is still observed in the measurements.

As with the *SRT*-modified method, it is assumed that the additional attenuation is due to the wet ice along the path. To correct for this additional attenuation first the HID algorithm is applied.

i. HID Results

The HID for this dataset was performed and areas with wet ice were detected. The results in Figure 4.3 show the detection of the wet ice core (denoted as wet graupel). The bottom panel plot shows the areas identified as wet graupel only. The hydrometeor identification was based herein using radar data in polar coordinates as opposed to gridding the radar data on a 3D Cartesian grid prior to classification. This is why the results look fuzzier than applying the algorithms to a gridded dataset.

As explained before, wherever 5 continuous gates were identified as wet graupel, the first gate in that sequence was used to identify the starting point to correct for the wet ice attenuated areas. Using this, the *PWF* correction was applied.

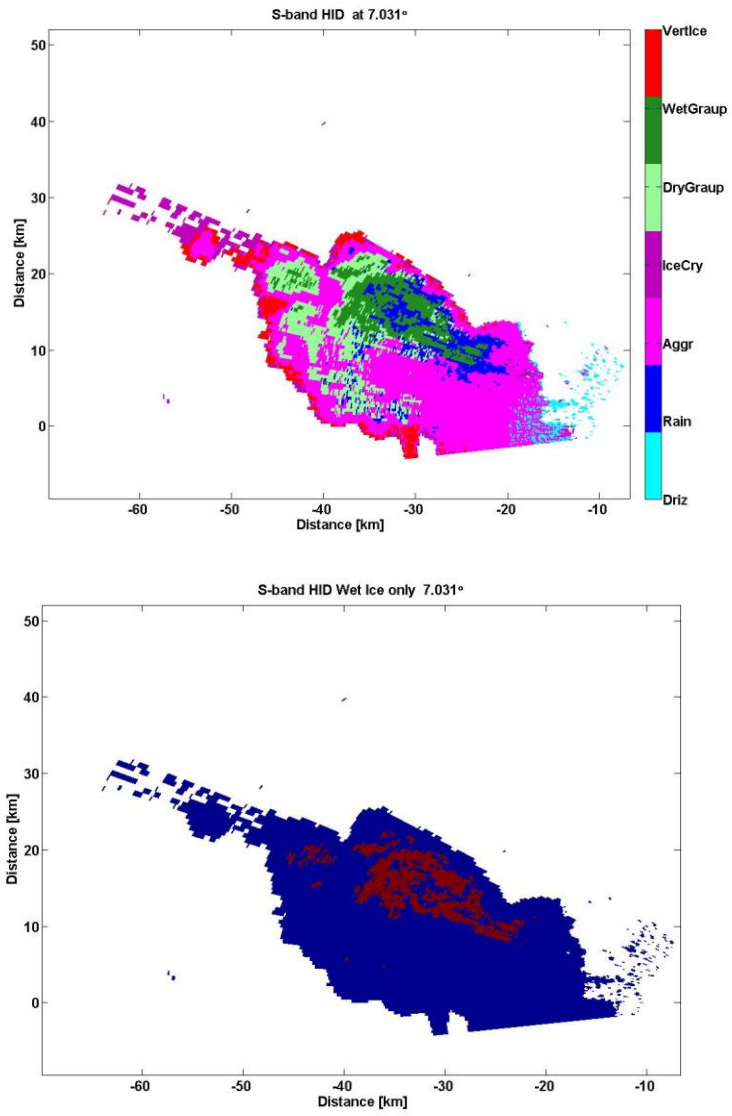

Figure 4.3: CP2 S-band HID results for the same PPI at 7° in elevation. Top panel have all the classifications and the bottom panel has only the wet graupel.

ii. PWF Correction Results

Once the HID is performed, the starting range gate is identified and the *PWF* attenuation correction method is used to correct the $Z_h(X)$ for the excess attenuation. The resulting PPI scan is shown in Figure 4.4. When compared with the $Z_h(S)$, the $Z_h(X)$ in the wet ice region is 'better corrected' than the one for the rain only correction (Figure 4.2). Areas with high reflectivities are

observed with the un-attenuated reflectivity values around the 55 dBZ as expected for wet ice regions.

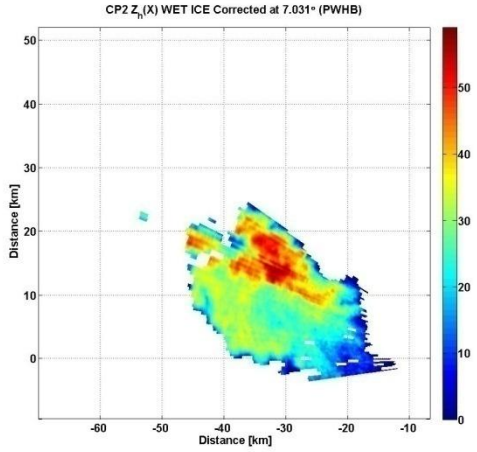

Figure 4.4: Resulting $Z_h(X)$ PPI scan after both rain and wet ice corrections at 7° in elevation.

The top panel of Figure 4.5 shows the range profiles of the reflectivities with the rain and wet ice attenuation corrections. When corrected for rain, the $Z_h(X)$ is still attenuated when compared to the un-attenuated $Z_h(S)$ profile. As with the previous method, it is assumed that this excessive attenuation is due to the wet ice along the propagation path. For this profile, the wet ice specific attenuation $A_h(X)^{wet\ ice}$ estimation and correction worked well, resulting in a comparable reflectivity with the $Z_h(S)$. On the other hand, another example beam in Figure 4.5, bottom panel, shows that the wet ice specific attenuation estimation and correction was not enough to be comparable with the un-attenuated $Z_h(S)$. Recall that the values for α and β used were selected as in Table 4.1 which represents 'average' values. The results in Figure 4.5 bottom panel suggest that for this specific beam, the α and β values needed for a more accurate correction should deviate from the 'average' values. The spatial variability of wet graupel correction is to be expected given that it depends on the size distribution, water coat thickness, etc. These results are comparable to those presented with the *SRT*-modified correction method (see Figure 3.20). The high reflectivity core has the expected values when wet ice is present.

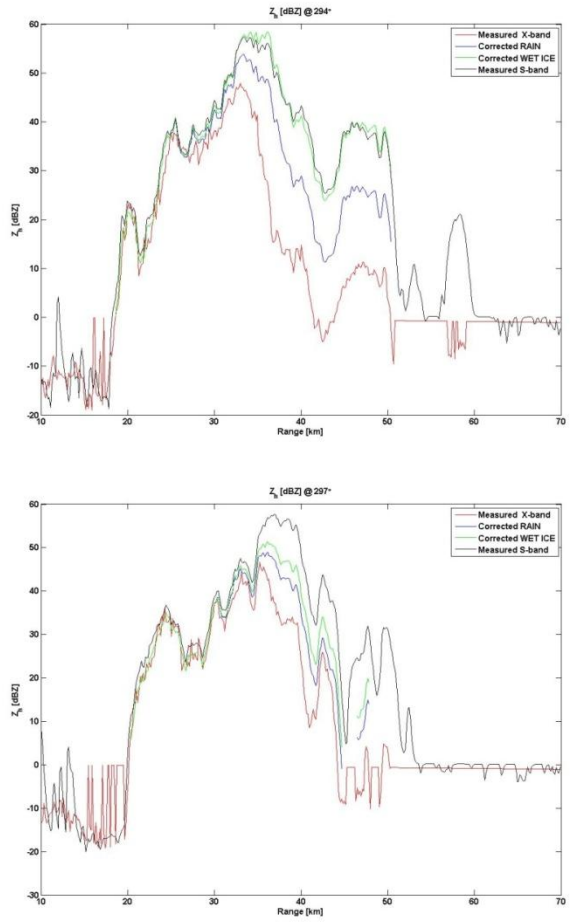

Figure 4.5: The top panel shows the $Z_h(X)$ range profiles with corrections applied at 294° in azimuth. The bottom panel shows the same for 297° in azimuth (under correction). For both of them the Mie 'hail' signal was removed.

One drawback from this method is that it depends greatly on the reflectivity that was already corrected for rain and reliable HID results on locating where the wet ice is located. If for some reason the HID wrongfully identifies an area with wet ice, the corrected reflectivity will result in an over correction, as shown in Figure 4.6. The profiles at 6° in elevation with the corrections shows that the reflectivity corrected for rain appears to be enough correction considering that the differences between the $Z_h(X)$ and $Z_h(S)$ are between -2 to 4 dBZ. Apparently the HID algorithm identified an area with wet ice, activating the wet ice attenuation correction. The results show an over correction of the $Z_h(X)$ given that the values are higher than 5 dB difference with un-attenuated $Z_h(S)$ and that clearly the rain corrected $Z_h(X)$ is comparable to $Z_h(S)$.

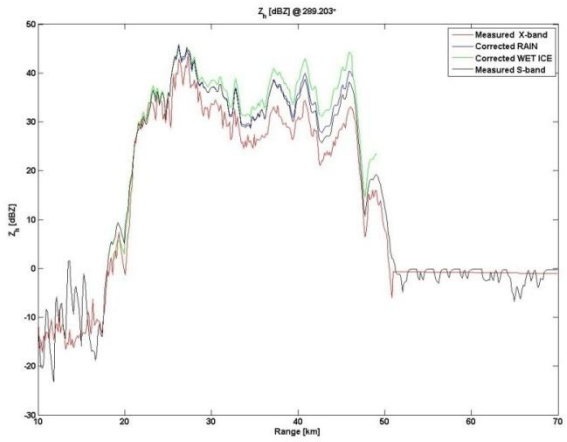

Figure 4.6: $Z_h(X)$ range profiles with corrections applied at 289° in azimuth (overcorrection) with the Mie 'hail' signal removed.

Another drawback from this method is that when the (equation 13) term is equal or higher than one, the attenuation estimation becomes unstable. This is usually achieved when the path integrated attenuation *PIA* exceeds the 15 dB (Delrieu, 1999).

Other than assuming a general $A_h(X)$-$Z_h(X)$ power law relationship, it is also assumed that the location of the first range bins containing wet ice are not highly attenuated as explained before. This allows the HID algorithm to correctly identify the beginning of a wet ice cores.

C. CASA07B Event

This event was previously analyzed using the *SRT*-modified method and the results are described in Chapter III. Now it is examined applying the *PWF* correction method.

i. HID Results

The HID results are shown in Figure 4.7, where all the classifications are included. The PPI scan at 12.25° is the same as the one analyzed in Chapter III. This is done to further compare results from both methods. As mentioned before, the HID algorithm is applied to the PPI scans rather

than the gridded data, since the *PWF* is a ray based correction method. This is why the HID results look fuzzier than gridded results which look smoother (see Figure 3.13). It is observed that areas with wet graupel are detected. These areas are the ones corrected by the *PWF* correction method. But one purpose behind this correction is whether highly attenuated cells in fact affects the HID results and if the wet ice attenuation correction helps identify better a wet ice core.

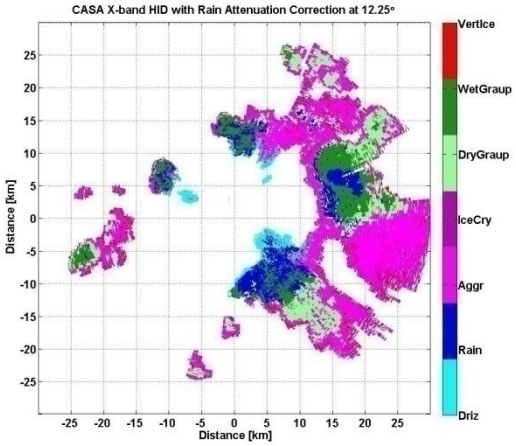

Figure 4.7: HID results for the CASA07B event with all the classifications included. Rain corrected $Z_h(X)$ is used here.

ii. PWF Correction Results

In Figure 4.8, the top panel shows the wet ice correction results. In the bottom panel, a section of the top panel was zoomed and the retrieved wet ice specific attenuation contours are included. With the *PWF* method, a maximum of $A_h(X)^{wet\ ice}$ of 1 dB km^{-1} is found. When compared with the *SRT*-modified method which had a maximum of 5 dB km^{-1}, the *PWF* method shows to be underestimating the wet ice specific attenuation. It did correct some of the attenuation but not all of it given that previously with the *SRT*-modified method it was found that higher attenuations were affecting the reflectivity values.

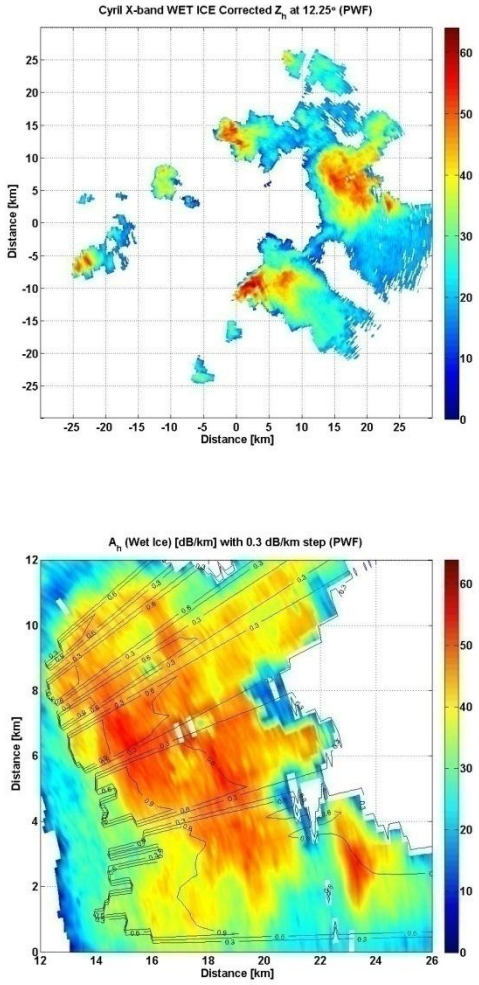

Figure 4.8: Wet ice attenuation corrected $Z_h(X)$. Top panel shows the whole scan at 12.25° and the bottom panel shows a section with the retrieved $A_h(X)^{wet\ ice}$ contours.

The $Z_h(X)$ corrected profile at azimuth angle of 58° is shown in Figure 4.9. With this dataset, different from the CP2 case, we do not have an un-attenuated reference profile to compare with. Still, it can be compared with Figure 3.15 where the same CASA data is corrected using the *SRT*-modified method and later with Figure 4.12 (bottom panel) where the networked based (attenuation correction method as described by Lim and Chandrasekar (2009) corrected the reflectivity for the same area. In this specific ray a maximum of 2 dB difference is observed.

Other rays from the volume scan (not shown here, but for example located at 67° in azimuth) presented corrections with maximum of 7.5 dB at most.

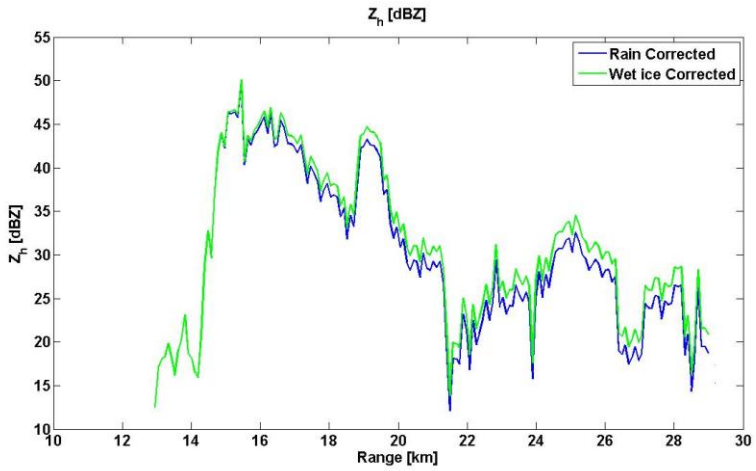

Figure 4.9: $Z_h(X)$ for rain and wet ice attenuation corrected range profiles at 58° in azimuth.

iii. HID Results after Correction: PWF and SRT-modified

To compare the effect of the *PWF* wet ice correction method in hydrometeor classification, the corrected data were also used for re-classification. Figure 4.10 shows the HID results for the wet ice corrected scan using the $Z_h(X)$ corrected for wet ice that resulted from the *PWF* method. Figure 4.11 right panel shows a section of Figure 4.7 and the left panel shows a section of Figure 4.10. It is needed to clarify that the only difference between the two is the reflectivity used. The other variables like the $Z_{dr}(X)$, $K_{dp}(X)$, and $\rho_{hv}(X)$ remained the same for both of the classifications. The third panel shows the classification result for the corrected $Z_h(X)$ complete scan. Some areas of wet ice are now identified as such while they were misclassified before the wet ice correction. This is due to the reflectivity increase in value with the wet ice correction and having in mind that the reflectivity variable is the one with more weight in the hydrometeor classification algorithm.

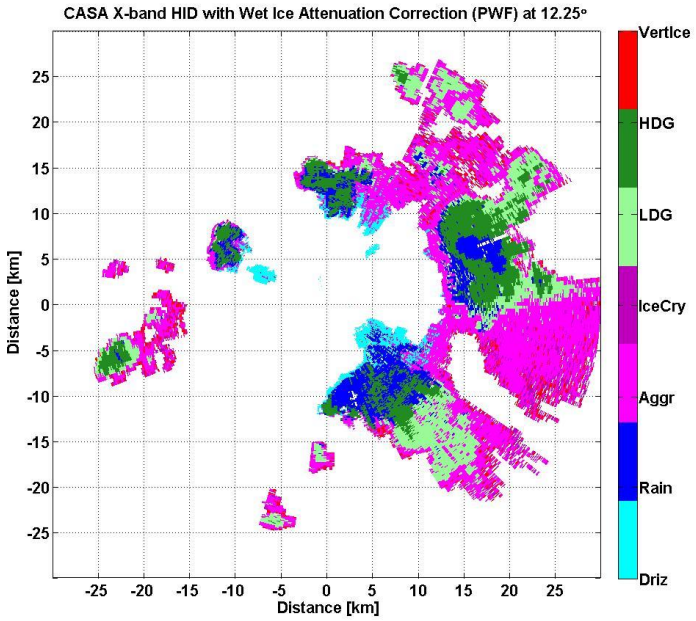

Figure 4.10: HID for the CASA07B event at 12.25° using the $Z_h(X)$ corrected for wet ice that resulted from the *PWF* method.

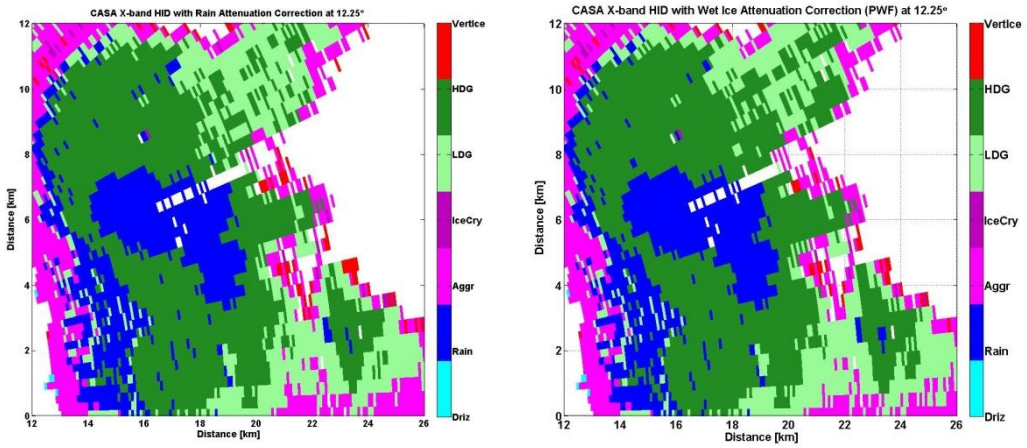

Figure 4.11: HID for the CASA07B event at 12.25°. Right panel shows the HID using the $Z_h(X)$ corrected for rain and the left panel shows the HID using the $Z_h(X)$ corrected for wet ice using the *PWF* method.

The results using the *SRT*-modified correction methods were classified too. Figure 4.12 show that after using this correction method the wet ice core is better identified than using the *PWF* method. Even though it still looks fuzzy it looks more like a core rather than selected pixels as before the

correction. It looks more 'realistic' since wet ice areas are found in a continuous way and not scattered along the beam path. These results show a better classification than the *PWF* results.

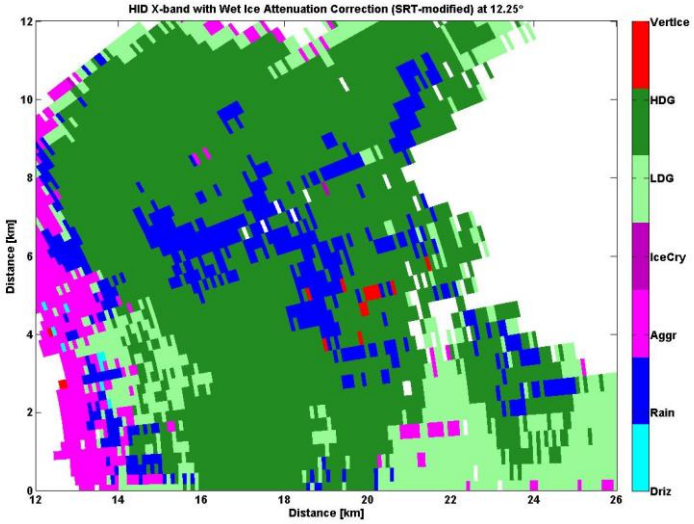

Figure 4.12: CASA X-band HID results using the *SRT*-modified correction method at 12.25°.

iv. Piece Wise Forward vs. Networked Based Correction

Another way to compare the results from the *PWF* correction method when correcting the CASA data is to use the network-based correction method. Figure 4.13 shows an area corrected with the *PWF* method in the top panel. The bottom panel shows same area with the *NB* corrected $Z_h(X)$. The *NB* results show higher reflectivities than the *PWF* method. The only drawback from the *NB* correction method is that it can only correct the attenuation for areas in common with at least three of the four CASA radars. The areas outside these common areas are subject to the current attenuation correction method that only corrects for rain attenuation. In addition, the *NB* method does not distinguish between rain and wet ice regions.

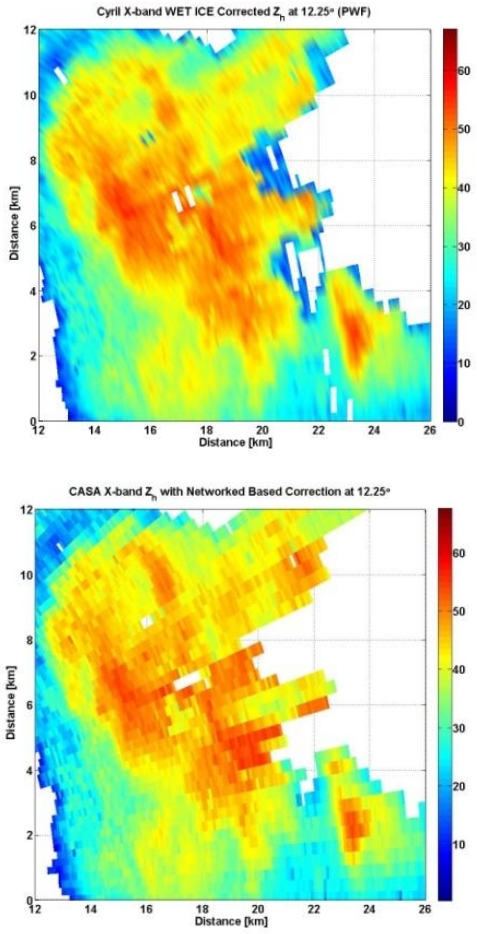

Figure 4.13: Piece-Wise Forward (*PWF*) and Network Based (NB) corrected $Z_h(X)$ results.

CHAPTER V

V. SUMMARY AND FUTURE WORK

A. Summary

At short wavelengths (typically less than 3 cm), weather radar signals are strongly attenuated by the precipitation along the signal path. These paths may contain different particles such as raindrops and melting ice which are the major contributors to high attenuation at X-band frequency. This constitutes a major source of error for radar rainfall estimation (when reflectivity is used as in *Z-R* relations), particularly for intense events like convective storms. This is the main reason why the total attenuation correction is an important step prior to quantitative rain estimation and hydrometeor identification. However, if the only application is rainfall estimation, then the differential propagation phase method does not suffer from attenuation as long as the *SNR* is sufficient.

This research was developed with the X-band CASA networked radars in mind. Presented are two possible solutions to correct for wet ice induced attenuation given that the current algorithms are Φ_{dp} based, which can only correct for rain attenuation. One of the solutions (*SRT*- modified) requires a (un-attenuated) reference signal, requiring two separate radars. The wet ice attenuation correction algorithm for X-band reflectivity was used in both simulated and measured radar data. From the CSU RAMS supercell simulation results it was observed that rain attenuation corrected profiles showed that additional (excess) attenuation is needed when compared with the un-attenuated reference signal. The *SRT*-modified method was applied and the resulting corrected

reflectivity profile showed good agreement with the un-attenuated signal (S-band). This algorithm was also applied to XPOL/SPOL data, CASA data and CP2 data, all with good agreement with the reference signal. Also, while applying this algorithm, wet ice specific attenuation was retrieved. Simulation results showed that the results were comparable to the 'true' simulated values and specific attenuation contours of wet ice coincided with areas of very high reflectivity (both S-band and corrected X-band) as expected in these cases. Rain specific attenuation was retrieved as well. This was done for all the events analyzed so far.

Given that for the CASA networked radars a reference might not always be available, a second wet ice correction method was developed. The second solution is based on a combination of a hydrometeor classification to identify where the wet ice is located and a priori $A_h(X)^{wet\ ice}$-$Z_h(X)$ relation. The latter power law relation was derived from CP2 radar measurements in a severe hailstorm. With these two results, a Piece Wise Forward method based on the Hitschfeld-Bordan solution was used to correct for the estimated wet ice attenuation. This method was tested with two different datasets. The same CP2 dataset used with the *SRT*-modified method was studied. It performed relatively well when compared with the first method, resulting in higher reflectivity values than those presented by the rain attenuation correction. With the CASA07B dataset, the method showed to underestimate the wet ice attenuation compared with the *SRT*-modified and *NB* one, although some areas showed reflectivity corrections up to 7.5 dB.

This research has shown that the Φ_{dp} based methods are not sufficient to correct for all the induced attenuation when wet ice is present. Two different techniques were able to successfully estimate the wet ice attenuation separately from that of rain. The *SRT*-modified method showed better agreement with the non-attenuated references than the *PWF* method. Although not demonstrated herein, the *PWF* has the limitation of failing when high *PIA* occurs. The *SRT*-modified method depends on having an un-attenuated reference and the *PWF* depends on successfully identifying where the wet ice areas are located. With both methods, we also

investigated the influence of the wet ice attenuation correction in successfully identifying hydrometeors and how well it compared with other methods. This makes the methods more useful in terms of having accurate data when using HID algorithms.

D. Future Work

It would be important to compare the wet ice attenuation correction methodology presented here using the CASA radars with un-attenuated S-band KOUN data using a large database. This way we can have a better idea on how well these methods perform in a statistical manner. A large database of dual-wavelength (S/X-band) data in HID classified mixed phase regions is also needed to develop robust attenuation-reflectivity power law relations for the *PWF* method or for the network based method. The modified *SRT* method is currently not suitable for real time applications for the CASA radars due to lack of an un-attenuated reference (though it could be provided by the NEXRAD network). At the current time the *PWF* method could be applied in real-time for the CASA radars using the HID classification of wet ice regions and the Hitschfeld-Bordan solution, mainly for low *PIA*s (less than 10 dB or so). Other methods that propose a backward implementation approach of the Hitschfeld-Bordan solution can also be explored along with the *A-Z* relations from the dual-wavelength radar determined in this work. This will eliminate the high *PIA* limitation and make the *PWF* more suitable for real-time application. It may also be that the microphysics that control wet ice attenuation might be so complicated as to preclude accurate attenuation-correction under all conditions without an un-attenuated reference beam.

REFERENCES

Anagnostou, E. N., Anagnostou, M. N., Krajewski, W. F., Kruger, A., Miriovsky, B. J., 2004: High-Resolution Rainfall Estimation from X-Band Polarimetric Radar Measurements, J. of Hydromet., 5, Issue 1, 110–128

Atlas, D., W. G. Harper, F. H. Ludlam, W. C. Macklin, 1960: Radar scatter by large hail. *Quart. J. Roy. Meteor. Soc.*, **86**, 468.

Atlas, D. and F. H. Ludlam, 1961: Multi-wavelength radar reflectivity of hailstorms. *Quart. J. Roy. Meteor. Soc.*, **87**, 523-534.

Aydin, K., T.A. Seliga and V. Balaji, 1986: Remote Sensing of Hail with a Dual Linear Polarization Radar. *J Appl Meteor.*, **25**, pp 1475–1484.

Battan, L. J., S. R. Browning and B. M. Herman, 1970: Attenuation by microwaves by wet ice spheres. *J. Appl. Meteor*., **9**, 832-834.

Battan, L. J., 1971: Radar attenuation by wet ice spheres. *J. Appl. Meteor*., **10**, 247-252.

Battan, L. J., 1973: Radar Observation of the Atmosphere. University of Chicago Press, 324 pp.

Bean, B. R., and E. J. Dutton, 1968: Radio Meteorology, Dover Publications, Inc. New York.

Bringi V. N., R. M. Rasmussen, and J. Vivekanandan, 1986a: Multiparameter radar Measurements in Colorado convective storms. Part I: Graupel melting studies. *J. Atmos. Sci.*, **43**, 2545–2563.

Bringi V. N., J. Vivekanandan, and J. D. Tuttle, 1986b: Multiparameter radar measurements in Colorado convective storms. Part II: Hail detection studies. *J. Atmos. Sci.*, **43**, 2564–2577.

Bringi, V.N., V. Chandrasekar, N. Balakrishnan, and D.S. Zrnić, 1990: An examination of propagation effects in rainfall on radar measurements at microwave frequencies. *J. Atmos. Oceanic Technol*., **7**, 829-840.

Bringi, V.N. and A. Hendry: Technology of Polarization Diversity Radars for Meteorology. In *Radar in Meteorology*. D. Atlas, Ed., 153-190, Boston, MA, American Meteorological Society, 1990.

Bringi, V.N. and V. Chandrasekar, 2001: Polarimetric Doppler Weather Radar: Principles and Applications. Cambridge.

Bringi, V.N., G. J. Huang, P. T. May, K. Glasson, and T. D. Keenan, 2009: The estimation of X-band attenuation due to wet ice in the mixed phase region of convective storms and correction of LDR at X-band using the CP-2 radar. *34th Conference on Radar Meteorology*, Williamsburg, VA. Amer. Meteor. Soc., Paper 11A.3.

Brotzge, J., K. Brewster, B. Johnson, B. Philips, M. Preston, D. Westbrook, and M. Zink, 2005: CASA's first test bed: Integrative Project #1 (IP1). *32nd Conference on Radar Meteorology*, Albuquerque, NM.

Carte, A. E., and G. Held, 1978: Variability of hailstorms on the South African plateau. *J. Appl. Meteo.*, **17**, 365-373.

Douglas, R. H., 1964: Hail size distribution. *Proc. Eleventh Wea. Radar. Conf.*, Boulder, Colo., Amer. Meteor. Soc., 146-149.

Delrieu, G., Caoudal, S., and Creutin, J.-D., 1997: Feasibility of using mountain return for the correction of ground-based X-band weather radar data, *J. Atmos. Oceanic Technol*., 14, 368–385.

Delrieu, G., Hucke, L., and Creutin, J., 1999: Attenuation in rain for X and C-band weather radar systems: sensitivity with respect to the drop size distribution, *J. Appl. Meteorol.*, 38, 57–68.

Eccles, P. J., and E. A. Atlas, 1973: A dual wavelength radar hail detector. *J. Appl. Meteor*., **12**, 847-854.

Eccles, P. J. 1975: Developments in Radar Meteorology: National Hail Research Experiment to 1973. *Atmos. Technol*., Winter, 1974-75, 34-35.

Eccles P. J., 1979, "Comparison of remote measurements by single and dual-wavelength meteorological radars, *IEEE Trans. Geophys. Electron*., vol.17, pp.205-208

Fraile et al., R. Fraile, A. Castro, L. López, J.L. Sánchez and C. Palencia, 2003: The influence of melting on hailstone size distribution, *Atmos. Res.* **67–68**, pp. 203–213.

Gorgucci, E., G. Scarchilli, and V. Chandrasekar, 1996: Error structure of radar rainfall measurement at C-band frequencies with dual-polarization algorithm for attenuation correction. *J. Geophys. Res.*, **101**, 26461-26471.

Gunn, K. L. S., and T.W. R. East, 1954: The microwave properties of precipitation particles. *Quart. J. Roy. Meteor. Soc*, **80**, 522-545.

Heymsfield A. J., A. R. Jameson, and H. W. Frank, 1980: Hail growth mechanisms in a Colorado storm: Hail formation processes. *J. Atmos. Sci.*, **37**, 1779–1807.

Hitschfeld W., and J. Bordan, 1954: Errors inherent in the radar measurements of rainfall at attenuating wavelengths. *J. Meteor*, **11**, 58–67.

Huang, G.J., V.N. Bringi, S. van den Heever, and W. Cotton, 2005: Polarimetric radar signatures from RAMS microphysics. *32nd Conference on Radar Meteorology*, Albuquerque, NM, Amer. Meteor. Soc., 24-29.

Iguchi, T., and R. Meneghini, 1994: Intercomparison of singe-frequency methods for retrieving a vertical rain profile from airborne or spaceborne radar data. *J. Atmos. Oceanic Technol*., **11**, 1507-1516.

Iguchi, T., T. Kozu, R. Meneghini, J. Awaka, and K. Okamoto, 2000: Rain-Profiling Algorithm for the TRMM Precipitation Radar. *J. Appl. Meteor.*, **39**, 2038-2052.

Jameson, A. R., and A. J. Heymsfield, 1980: Hail growth mechanisms in a Colorado Storm. Part 1: Dual-wavelength processing, *20th Conference on Radar Meteorology*, Boston, Massachusetts, Amer. Meteor. Soc., 676-682.

Keeler, R.J., B.W. Lewis and G.R. Gray, 1989: Description of NCAR/FOF CP2 Meteorological Doppler Radar. *24th Conf. on Radar Meteorology*, Tallahassee, Florida, Amer. Meteor. Soc., 589-592

Liu, Y., G.J. Huang, V.N. Bringi and S. van den Heever, 2006a: Estimation of X-band radar attenuation due to wet hail: A simulation study using RAMS supercell case and dual-wavelength (S/X-band) radar. *ERAD06*, 49-52.

Liu, Y., V. N. Bringi, and M. Maki, 2006b: Improved Rain Attenuation Correction Algorithms with Adaptation to Drop Shape Models, *IEEE International Geoscience and Remote Sensing Symposium 2006*, Denver, Colorado.

McLaughlin, D. J. et al., 2005: Distributed Collaborative Adaptive Sensing (DCAS) for improved detection, understanding, and predicting of Atmospheric hazards, in *Proc. of 85th AMS Annual Meeting, San Diego, California.*

Lim, S. and Chandrasekar, V., 2009: Evaluation of networked based attenuation correction in CASA IP1 testbed. *34th Conference on Radar Meteorology*, Amer. Meteor. Soc., Williamsburg, VA. Paper 2.26.

Marshall, J. and W. Palmer, 1949: The distribution of raindrops with size. *J. Meteorology*, ***5***, 165-166.

Matrosov, S.Y., K.A. Clark, B.E. Martner, and A. Tokay, 2002: X-band polarimetric radar measurements of rainfall. *J. Appl. Meteor.*, **41**, 941-952.

Meneghini, R., J. Eckerman, and D. Atlas, 1983: Range profiling of the rain rate by an airborne weather radar. *Remote Sens. Environ*., **31**, 193-209.

Meyers, M. P., R. L. Walko, J. Y. Harrington, W. R. Cotton, 1997: New RAMS cloud microphysics parameterization. Part II: The two-moment scheme. *Atmos. Res.*, **45**, 3-39.

Park, S.G., V.N. Bringi, V. Chandrasekar, M. Maki and K. Iwanami, 2005: Correction of radar reflectivity and differential reflectivity for rain attenuation at X band. Part I: theoretical and empirical basis. *J. Atmos. Oceanic Technol.*, **22**, 1621-1632.

Park, S.G., M. Maki, K. Iwanami, V.N. Bringi and V. Chandrasekar, 2005: Correction of radar reflectivity and differential reflectivity for rain attenuation at X band. Part II: evaluation and application. *J. Atmos. Oceanic Technol.*, **22**, 1633-1655.

Tabary, P., G. Vulpiani, J. J. Gourley, A. J. Illingworth and O. Bousquet, 2008: Unusually large attenuation at C-band in Europe: How often does it happen? What is the origin? Can we correct for it?. ERAD08.

Testud, J., E.L. Bouar, E. Obligis, and M. Ali-Mehenni, 2000: The rain profiling algorithm applied to polarimetric weather radar. *J. Atmos. Oceanic Technol.*, **17**, 322-356.

Tuttle, J.D. and R.E. Rinehart, 1983: Attenuation correction in dual-wavelength analyses. *J. Climate Appl. Meteor.*, **22**, 1914-1921.

Sulakvelidze, G. K., 1965: Findings for the Caucasus anti-hail expedition (1965). [Translated from Russian by Israel Program for Scientific Translations, Jerusalem, 1967, 60pp.]

van den Heever, S.C., and W.R. Cotton, 2005: Modeling the impacts of urban aerosol on convection and precipitation, *16th Conference on Planned and Inadvertent Weather Modification*, AMS, San Diego, CA.

Vulpiani, G., P. Tabary, J. Prent-du-Chatelet, O. Bouquet, M. L. Segond, and F. S. Marzano, 2007: Hail detection using a polarimetric algorithm at C band: Impact on Attenuation Correction. *33rd Conference on Radar Meteorology*, Cairns, Australia, Amer. Meteor. Soc.

APPENDIX A

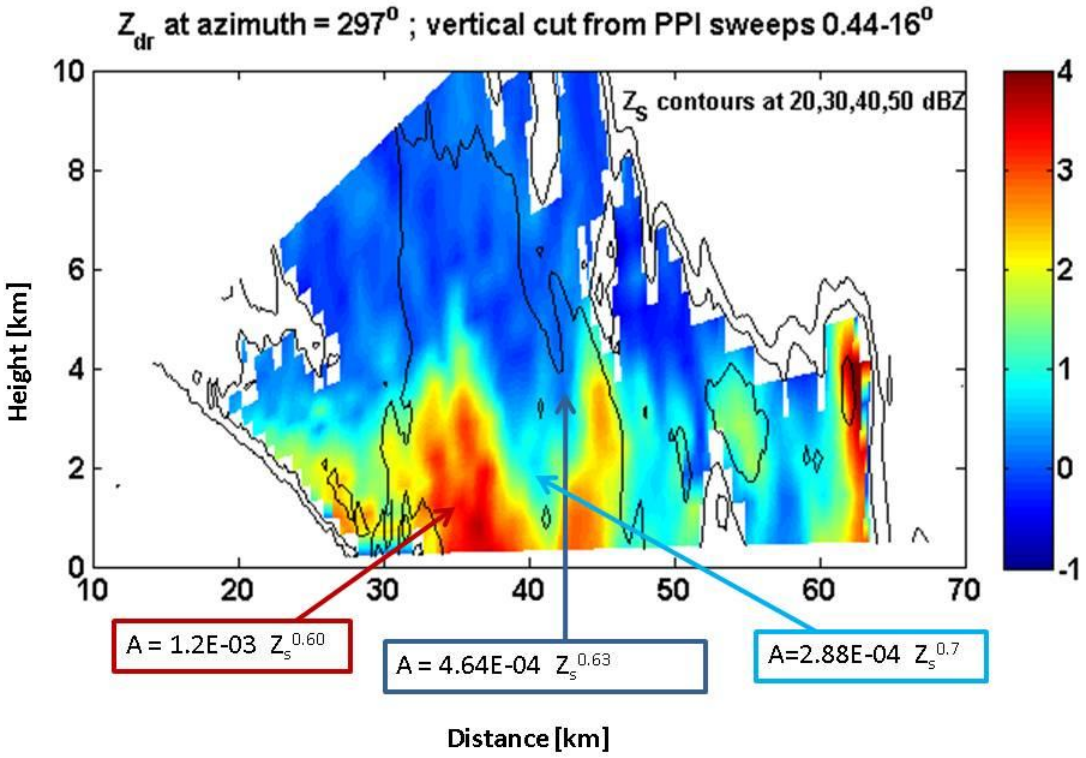
Z_dr at azimuth = 297° ; vertical cut from PPI sweeps 0.44-16°
Z_S contours at 20,30,40,50 dBZ
Height [km]
Distance [km]
A = 1.2E-03 Z_s^0.60
A = 4.64E-04 Z_s^0.63
A=2.88E-04 Z_s^0.7

LIST OF ABBREVIATIONS

CAPPI: constant altitude PPI

CASA: Collaborative Adaptive Sensing of the Atmosphere

CHILL: Chicago/Illinois State Water Survey

CP2: Cloud Physics radar

CSU: Colorado State University

CYR: CASA radar located in Cyril, Oklahoma

ERC: Engineering Research Center

HB: Hitschfeld and Bordan

HID: hydrometeor identification

HS: hail signal

IHOP: International H2O Project

IP1: Integrative Project 1

KOUN: NEXRAD radar located in Norman, Oklahoma

KTLX: NEXRAD radar located in Oklahoma City, Oklahoma

NB: network based

NCAR: National Center for Atmospheric Research

NEXRAD: Next generation Radars

NHRE: National Hail Research Experiment

NSF: National Science Foundation

NSSL: National Severe Storm Laboratory

NWS: National Weather Service

PIA: path integrated attenuation

PPI: plan position indicator

PWF: piece-wise forward

RAMS: Regional Atmospheric Modeling System

RHI: range height indicator

RSP: CASA radar located in Rush S prings, Oklahoma

SNR: signal to noise ratio

SPOL: S-band dual polarization radar

SRT: surface reference method

TRMM: Tropical Rain Measurement Mission

XPOL: X-band dual polarization radar